AD-A187 649 A SECOND ORDER GODUNOV METHOD FOR SUPERSONIC TACTICAL MISSILES(U) NAVAL SURFACE WEAPONS CENTER SILVER SPRING MD A B WARDLAW ET AL DEC 86 NSWC-TR-86-586 1/1

UNCLASSIFIED F/G 16/2.1 NL

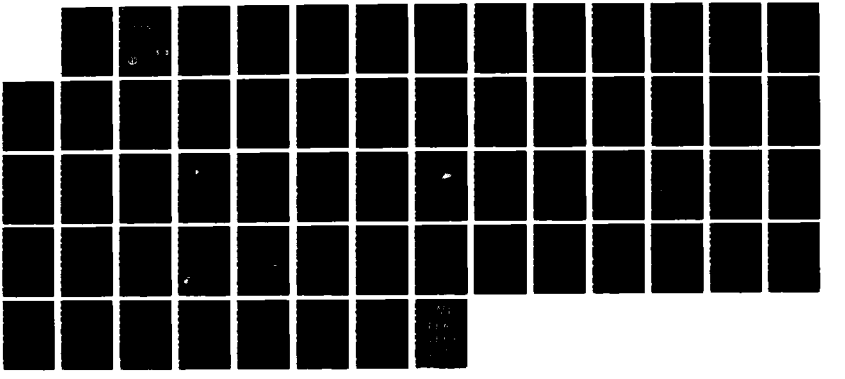

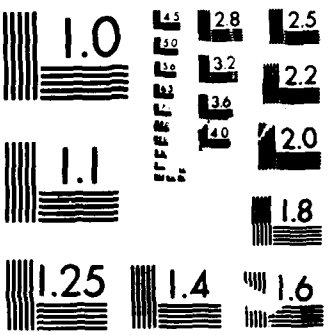

NSWC TR 86-506

A SECOND ORDER GODUNOV METHOD FOR SUPERSONIC TACTICAL MISSILES

BY A. B. WARDLAW, JR. S. F. DAVIS

RESEARCH AND TECHNOLOGY DEPARTMENT

DECEMBER 1986

NAVAL SURFACE WEAPONS CENTER

Dahlgren, Virginia 22448-5000 • Silver Spring, Maryland 20903-5000

REPORT DOCUMENTATION PAGE

1a REPORT SECURITY CLASSIFICATION Unclassified	1b RESTRICTIVE MARKINGS
2a SECURITY CLASSIFICATION AUTHORITY	3 DISTRIBUTION / AVAILABILITY OF REPORT Approved for public release; distribution is unlimited.
2b DECLASSIFICATION / DOWNGRADING SCHEDULE	
4 PERFORMING ORGANIZATION REPORT NUMBER(S) NSWC TR 86-506	5 MONITORING ORGANIZATION REPORT NUMBER(S)
6a NAME OF PERFORMING ORGANIZATION Naval Surface Weapons Center 6b OFFICE SYMBOL (If applicable) R44	7a NAME OF MONITORING ORGANIZATION Naval Air Systems Command
6c ADDRESS (City, State, and ZIP Code) 10901 New Hampshire Avenue Silver Spring, MD 20903-5000	7b ADDRESS (City, State, and ZIP Code) Attn: Code AIR-932J Crystal City, VA 20361-9320
8a NAME OF FUNDING / SPONSORING ORGANIZATION 8b OFFICE SYMBOL (If applicable)	9 PROCUREMENT INSTRUMENT IDENTIFICATION NUMBER
8c ADDRESS (City, State, and ZIP Code)	10 SOURCE OF FUNDING NUMBERS PROGRAM ELEMENT NO: 61153N PROJECT NO: SR023 TASK NO: SR023-02 WORK UNIT ACCESSION NO: R44AA

11 TITLE (Include Security Classification)
A Second Order Godunov Method for Supersonic Tactical Missiles

12 PERSONAL AUTHOR(S) Wardlaw, A. B., Jr., and Davis, S. F.

13a TYPE OF REPORT	13b TIME COVERED	14 DATE OF REPORT (Year, Month, Day)	15 PAGE COUNT
Summary	FROM 10/83 TO 12/86	1986 December	62

16 SUPPLEMENTARY NOTATION

17 COSATI CODES			18 SUBJECT TERMS (Continue on reverse if necessary and identify by block number)
FIELD	GROUP	SUB-GROUP	
16	04		

19 ABSTRACT (Continue on reverse if necessary and identify by block number)

A second order Godunov scheme is described for steady supersonic flow. This scheme, which marches the solution in space, is cast in a finite volume formulation and uses a mesh generated by a multiple zone procedure. Second order accuracy is obtained by computing local slopes and adding a predictor step. Both an approximate and a linearized version of the Riemann problem can be used to increase efficiency. The bow shock is fit using the information contained within the Riemann problem. The scheme is applied to both body alone and finned configurations for which experimental data is available. Reasonable agreement is obtained between experiment and calculation without the use of artificial viscosity or special procedures.

20 DISTRIBUTION / AVAILABILITY OF ABSTRACT	21 ABSTRACT SECURITY CLASSIFICATION
☒ UNCLASSIFIED/UNLIMITED ☐ SAME AS RPT ☐ DTIC USERS	Unclassified
22a NAME OF RESPONSIBLE INDIVIDUAL Andrew B. Wardlaw, Jr.	22b TELEPHONE (Include Area Code) 202-394-2265 22c OFFICE SYMBOL R44

★U.S. Government Printing Office: 1985—539-012

FOREWORD

A second order Godunov scheme is described for steady supersonic flow. This scheme, which marches the solution in space, is cast in a finite volume formulation and uses a mesh generated by a multiple zone procedure. Second order accuracy is obtained by computing local slopes and adding a predictor step. Both an approximate and a linearized version of the Riemann problem can be used to increase efficiency. The bow shock is fit using the information contained within the Riemann problem. The scheme is applied to both body alone and finned configurations for which experimental data is available. Reasonable agreement is obtained between experiment and calculation without the use of artificial viscosity or special procedures. This work was supported by Naval Surface Weapons Center Independent Research, Naval Sea Systems Command and Naval Air Systems Command. The project monitors were Dale Hutchins (AIR-310-C) and Lionel Pasiuk (SEA-62R41).

Approved by:

Carl W. Larson

CARL W. LARSON, Head
Radiation Division

CONTENTS

ILLUSTRATIONS

TABLE

SECTION 1

INTRODUCTION

The hyperbolic nature of the Euler equations in supersonic flow permits a solution by spatial marching. Here an initially known flow field on a crossflow plane near the missile nose is marched down the missile length. For a sharp tipped missile the initial flow field can be constructed from a conical solution while a blunt body solver must be used in the case of a blunt shape. The computation terminates when the base of the missile is reached or when subsonic regions are encountered.

This report describes the application of a second order Godunov method to tactical missile shapes (i.e., bodies with thin, low aspect ratio lifting surfaces). The grid is generated using a multiple zone method that divides the crossflow plane up into several quadrilateral zones. The body, fin, and tracked bow shock surfaces must lie on the zone edges. A typical zone structure for a body-wing missile is illustrated in Figure 1 while the quadrilateral zone geometry is shown in Figure 2. The numerical method is cast in control volume form and consists of a predictor and corrector step. The predictor step advances the primitive variables using Euler's equations in non-conservation form. Derivatives are computed using a limited central differencing procedure. The corrector step modifies Godunov's method by assuming linear property variations within each control volume.

The multiple zone computational procedure has been previously applied to missiles using a MacCormack type scheme with characteristic boundary conditions.[1,2] At wing edges and surface discontinuities, these boundary conditions are appended with special procedures which apply oblique shocks or expansions as appropriate. These methods have been successfully applied to missiles, but lack robustness. In simple cases (e.g., a tangent ogive at low incidence), accurate, efficient solutions are achieved. However, for more complicated shapes the user must adjust the artificial viscosity levels and special procedures. A first order Godunov method has also been developed using the multiple zone approach[3] which is extremely robust and devoid of special procedures. In regions where shocks occur these results are comparable to those obtained by the MacCormack scheme. However, on smooth bodies, accurate prediction of surface pressures can only be obtained with extremely fine meshes. This general recipe for constructing a second order accurate Godunov scheme was suggested in Reference 4. It has been applied to unsteady, compressible flow in References 5, 6 and 7 and to steady supersonic flow in References 8 and 9.

The second order Godunov scheme presented in this paper is imbedded in a multiple zone framework which features the division of the computational domain into quadrilateral zones of the type shown in Figure 2. The edges of

adjacent zones spacially coincide with one another and do not overlap. The quadrilateral zone must be consistent with the following constraints (see Figure 3 for zone numbering convention):

1. Edge 2 can only abut to edge 4. Edges 1 and 3 cannot abut to other edges.

2. Surfaces and symmetry planes must lie on zone edges.

3. Bow shocks which are to be fitted must lie on edge 3.

The geometry of the zone edges can be defined using either cylindrical or cartesian coordinates. These constraints are sufficiently loose to allow a large number of different internal or external flows to be handled. This includes body-wing-tail missiles, wings alone and inlet flows. Geometries including features such as detached inlets or a tail located on a wing require abutting edges 1 and 3, as well as 2 and 4. These types of shapes cannot be handled by the present second order Godunov code. Reference 2 describes a MacCormack based multiple zone method for computing such flows.

A user guide for the method described in this report is provided in Reference 9.

SECTION 2

THE RIEMANN PROBLEM

In steady supersonic flow the Riemann problem represents the confluence of two, two-dimensional supersonic streams, as is illustrated in Figure 4. At tne point of stream intersection, shocks and/or expansion fans form, turning both streams to a common direction. The appropriate direction is the one producing the same pressure in both streams. The two final streams need not feature the same density or velocity and a slip line usually forms between them. Solutions are self-similar in z and feature constant properties along any line passing through the point of initial stream intersection.

Figure 3 depicts the Riemann problem formed by the intersection of two streams with properties (p_+, ρ_+, u_+, w_+) and (p_-, ρ_-, u_-, w_-). Upward deflection of the (+) stream is described by the shock relations and leads to an increase in pressure while downward deflection is associated with an expansion and leads to a decrease in pressure. On the other hand, upward deflection of the (-) stream leads to an expansion and downward deflection to a shock. To solve the Riemann problem, it is necessary to determine the final flow direction, which produces the same final pressure in both streams. The shock and expansion equations define the relation between the two initial flow directions, $\delta_\pm$ and pressure, $p_\pm$, and final pressure and direction, p, δ. These can be written expressing δ as a function of $\delta_\pm$, $p_\pm$, and p:

$$\delta_f = \delta_\pm \pm \tan^{-1}\left\{\left[\frac{(p_f-p_\pm)}{(\gamma M_\pm^2+1)p_\pm - p_f}\right]^2\left[\frac{p_\pm(2\gamma M_\pm^2-\gamma+1) - (\gamma+1)p_f}{(\gamma+1)p_f+(\gamma-1)p_\pm}\right]^{1/2}\right\} \quad \begin{matrix}\text{:shock} \\ p_f > p_\pm\end{matrix} \qquad (1)$$

$$\delta_f = \delta_\pm \pm \nu(M_\pm) \mp \nu(M_f) \quad \begin{matrix}\text{:expansion} \\ p_f < p_\pm\end{matrix} \qquad (2)$$

where: $$M_f = \frac{2}{(\gamma-1)}\left[\left(\frac{p_\pm}{p_f}\right)^{\frac{\gamma-1}{\gamma}}\left(1+\frac{(\gamma-1)}{2}M_\pm^2\right) - 1\right]^{1/2}$$

$$\nu(M) = \bar{C}\tan^{-1}\left[\frac{(M^2-1)}{\bar{C}^2}\right]^{1/2} - \tan^{-1}[M^2-1]^{1/2}$$

$$\bar{C} = \left[\frac{(\gamma+1)}{(\gamma-1)}\right]^{1/2}$$

Here the upper and lower signs are associated with the (+) and (-) stream respectively. The resulting ($p - \delta$) curves for the + and - streams are graphed in Figure 4. The solution to the Riemann problem corresponds to the intersection of the two illustrated curves.

2.1 COMPLETE SOLUTION

The non-linearity of Eqs. (1) - (2) precludes a closed form solution. Instead, an iterative procedure is used which proceeds from step n to n+1 as follows:

1. At the start of iteration step n+1, two points are known on both the + and - (p-δ) curves: $(p_{\pm}^{n}, \delta_{\pm}^{n})$, $(p_{\pm}^{n-1}, \delta_{\pm}^{n-1})$. The equations for the lines passing through the two known points on each curve are determined.

2. The intersection of the two lines is determined and p is taken to be the pressure at the point of intersection.

3. δ_+ and δ_- are determined by evaluating Eqs. (1) and (2) using the value of p determined in step 2.

4. If $|\delta_+ - \delta_-| < 10^{-3}$, the iteration is terminated.

To start the iteration:

$$p_{\pm}^{0} = p_{\pm} , \qquad \delta_{\pm}^{0} = \delta_{\pm} , \; p_{\pm}^{1} = p_L . \tag{3}$$

Here p_L is the linearized pressure solution discussed in the next section. $\delta_{\pm}^{1}$ are determined by evaluating Eqs. (1) and (2) using P_L.

The Godunov procedure, which is described in Section 3.2, requires knowledge of the flow properties associated with a specific direction, θ_s. As indicated in Figure 3, three different regions, ($R_{\pm}$, F, E) are featured on the expansion side of a slip line and two ($R_{\pm}$, S) on the shock side. If θ lies in $R_{\pm}$, the initial conditions provide the needed properties. For θ lying in S or E, the variables p, δ are determined by the Riemann solution and the density is computed using the oblique shock relations:

$$\frac{\rho}{\rho_{\pm}} = \frac{(\gamma+1)M_{\pm}^{2}\sin^{2}\theta_{s_{\pm}}}{(\gamma-1)M_{\pm}^{2}\sin^{2}\theta_{s_{\pm}}+2} \tag{4}$$

$$\text{where:}\quad \sin^2\theta_{s_\pm} = [(\gamma+1)\frac{p}{p_\pm} + (\gamma-1)]/(2\gamma M_\pm^2) \tag{5}$$

In region E, the isentropic relations provide the correct density. However, the shock relation is less expensive to apply and yields the required accuracy. When θ lies in F, the flow direction δ along θ is given by:

$$\delta = \theta \mp \sin^{-1}\{\frac{1}{M^*}\} \tag{6}$$

Here M^* is the Mach number along the direction θ. Using Eq. (2):

$$\delta_\pm \pm \nu(M_\pm) = \theta \pm \nu(M^*) \mp \sin^{-1}\{\frac{1}{M^*}\} \tag{7}$$

and solving for M^* yields: (8)

$$M^* = [1 + \bar{C}^2 \tan^2\{\frac{\pi/2 + \nu(M_\pm) \pm (\delta_\pm - \theta)}{\bar{C}}\}]^{1/2}$$

With M^* known, the remaining properties along θ follow immediately from the isentropic relations.

The angle between the shock and the slip line, θ_s, is given in Eq. (5), while the angle between the slip line and the head and tail characteristics of the expansion fan are the characteristic angles, based on the Mach number upstream and downstream of the fan respectively.

2.2 APPROXIMATE SOLUTIONS

Approximate, closed form solutions to the Riemann problem can be obtained in cases featuring similar + and - states. This often circumvents the need to use an iterative method. To develop approximate solutions, the shock relation, Eq. (1), is expanded in the following Taylor series:

$$p = p_\pm \pm k_{1_\pm}(\delta-\delta_\pm) + k_{2_\pm}(\delta-\delta_\pm)^2 \pm k_{3_\pm}(\delta-\delta_\pm)^3 + O[(\delta-\delta_\pm)^4] \tag{9}$$

$$\text{where:}\quad k_{1_\pm} = p_\pm \gamma M_\pm^2/(M_\pm^2-1)^{1/2}$$

$$k_{2_\pm} = p_\pm \gamma M_\pm^2\left[\frac{(\gamma+1)M_\pm^4 - 4(M_\pm^2-1)}{4(M_\pm^2-1)^2}\right]$$

$$k_{3_\pm} = \frac{p_\pm \gamma M_\pm^2}{(M_\pm^2-1)^{7/2}} \left[\frac{(\gamma+1)^2}{32} M_\pm^8 - \frac{(7 + 12\gamma - 3\gamma^2)}{24} M_\pm^6 + \frac{3}{4}(\gamma+1)M_\pm^4 - M_\pm^2 + \frac{2}{3} \right]$$

The Prandtl-Meyer expansion series is identical to the above through second order. The third order terms, for γ=1.4, are typically within 10% of each other, and Eq. (9) will be used to represent both shocks and expansions. Retaining only linear terms and requiring that the final upper and lower stream pressures be equal yields the linear solution:

$$p_L = p_+ + \frac{k_{1_+}\{[p_- - p_+] + k_{1_-}[\delta_- - \delta_+]\}}{(k_{1_+} + k_{1_-})}$$

$$\delta_L = \delta_+ + \frac{\{(p_- - p_+) + k_{1_-}(\delta_- - \delta_+)\}}{(k_{1_+} + k_{1_-})} \tag{10}$$

This estimate can be improved by considering the second order term in Eq. (6). Let δ_Q be the quadratic solution and write:

$$\delta_Q - \delta_\pm = (\delta_Q - \delta_L) + (\delta_L - \delta_\pm) = \Delta\delta_Q + \Delta\delta_{L_\pm} \tag{11}$$

Substituting the above into Eq. (9), and dropping the $\Delta\delta_Q^2$ term results in:

$$p = p_{L_\pm} + k_{2_\pm}\Delta\delta_L^2 + \Delta\delta_Q[\pm k_{1_\pm} + 2k_{2_\pm}\Delta\delta_{L_\pm}] \tag{12}$$

Equating the upper and lower stream pressures yields:

$$\Delta\delta_Q = (k_{2_-}\Delta\delta_{L_-}^2 - k_{2_+}\Delta\delta_{L_+}^2)/(2k_{2_+}\Delta\delta_{L_+} - 2k_{2_-}\Delta\delta_{L_-} + k_{1_+} + k_{1_-}) \tag{13}$$

The final pressure can be evaluated to second or third order using Eq. 9.

Properties along a direction θ are evaluated using the same procedure discussed in the preceding section, except in the linear case. Here the Riemann solution is assumed to contain two distinct regions separated by lines along which flow properties are discontinuous, as is illustrated in Figure 5. In particular, it is assumed that expansion fans are infinitely thin.

The efficiency of the Riemann problem strongly impacts that of the Godunov procedure. To minimize the computational resources devoted to the Riemann problem, the approximate solution is calculated as follows:

1. The linear pressure and flow direction are determined from Eq. 7.

2. If max ($|\delta_L-\delta_+|$, $|\delta_L-\delta_-|$) < .02, the linear solution is used as the final Riemann solution.

3. If max ($|\delta_L-\delta_+|$, $|\delta_L-\delta_-|$) > .02, the quadratic solution is evaluated from Eq. 13.

4. If .02 < max ($|\delta_q-\delta_+|$, $|\delta_q-\delta_-|$) < .06, the pressure, p_q, is evaluated using first and second order terms of Eq. 9. Slightly different p_q values are obtained from the upper and lower streams. The final pressure is an average of $p_{q_\pm}$.

5. If .06 < max ($|\delta_q-\delta_+|$, $|\delta_q-\delta_-|$) < .10, the first, second and third order terms of Eq. 9 are used to calculate pressure, p_c. p_{c_+} and p_{c_-} are averaged to determine the final pressure.

6. If max ($|\delta_q-\delta_+|$, $|\delta_q-\delta_-|$) > .10, the iterative procedure outlined in the last section is applied.

2.3 APPROXIMATE PROBLEM

An alternative to obtaining an approximate solution to the supersonic Riemann problem is to define an approximate Riemann problem which can be readily solved. Following the general approach outlined by Davis for conservation laws, a simplified Riemann problem for supersonic flow can be constructed.[7] It features a single set of intermediate properties separating the two initial states as is shown in Figure 6. The slopes, $\bar{a}^+$ and $\bar{a}^-$, of the two surfaces across which flow properties are discontinuous, are defined as follows:

$$\bar{a}^+ = \min(\lambda_-^+, \lambda_-^-), \quad \bar{a}^- = \max(\lambda_+^+, \lambda_+^-) \tag{14}$$

where: the subscript refers to the root
the superscript refers to the + or - stream

$$\lambda_\pm^\pm = \frac{wu \pm a\sqrt{u^2+w^2-a^2}}{w^2 - a^2} \tag{15}$$

The parameters $\bar{a}_\pm$ are easily computed and ensure that the complete Riemann problem wave speeds are faster than $\bar{a}_-$ and slower than $\bar{a}_+$. This assures that the entropy condition is satisfied and that the method converges to the correct physical solution.[7,10,11]

The intermediate state, denoted by a superscript asterisk, is calculated by balancing mass and momentum fluxes through the dashed control volumes of Figure 6. A quadratic equation must be solved to determine the primitive

variables p, ρ, u, w. However, the information necessary for the Godunov scheme is simply the fluxes normal to some direction, θ, as shown in Figure 6:

$$\bar{F}^{*} = \begin{bmatrix} \rho^{*} v_n^{*} \\ \rho^{*} v_n^{*} w^{*} + p^{*} \cos\theta \\ \rho^{*} v_n^{*} u^{*} + p^{*} \sin\theta \end{bmatrix} . \qquad (16)$$

Here v_n^* is the velocity normal to the θ = constant plane. $\bar{F}^{*}$ can be computed directly without the need to determine the primitive variables. To accomplish this, conservation is satisfied for the two dotted control volumes shown in Figure 7. This yields the following vector equation:

$$\begin{aligned} a^{+}U^{*} &= a^{+}U^{+} - \frac{F^{+}}{\cos\theta} + \frac{F^{*}}{\cos\theta} \qquad \text{upper control volume} \\ -a^{-}U^{*} &= -a^{-}U^{-} + \frac{F^{-}}{\cos\theta} - \frac{F^{*}}{\cos\theta} \qquad \text{lower control volume} \end{aligned} \qquad (17)$$

where: $a^{+} = \tilde{a}^{+} - \tan\theta$

$a^{-} = \tilde{a}^{-} - \tan\theta$

Solving for $\bar{F}^{*}$ produces:

$$F^{*} = \frac{a^{-}a^{+}(U^{+} - U^{-})\cos\theta + a^{+}F^{-} - a^{-}F^{+}}{(a^{+} - a^{-})} \qquad (18)$$

When applying the approximate Riemann solution to the Godunov scheme, it is necessary to determine F along some arbitrary direction θ.

If $\tilde{a}^{-} < \tan\theta < \tilde{a}^{+}$, the above flux definition is the appropriate one. However, for $\tan\theta > \tilde{a}^{+}$ or $\tan\theta < \tilde{a}^{-}$, the F^{+} and F^{-} fluxes, respectively, must be used. This can be accomplished using the above formula if a^{+} and a^{-} are redefined as follows:

$$\begin{aligned} a^{+} &= \max(\tilde{a}^{+} - \tan\theta, 0) \\ a^{-} &= \min(\tilde{a}^{-} - \tan\theta, 0) \end{aligned} \qquad (19)$$

SECTION 3

NUMERICAL METHOD

3.1 ZONE DESCRIPTION

In the crossflow planes z = constant, zones are generalized quadrilaterals as shown in Figure 2. Each zone is described with respect to (s, τ, ν) coordinates, which either represent cylindrical (r, ϕ, z) or cartesian (x, y, z) coordinates (see Figure 7). Cylindrical coordinates facilitate treatment of wing-body configurations, while cartesian coordinates can be applied to wing alone cases. The numbering system used to designate the edges and corners of a zone are indicated in Figure 2. The locations of edges 1 and 3 are defined by the functions $b(\tau, \nu)$, while the coordinates of edges 2 and 4 are defined by $\Psi(s, \nu)$, and $\sigma(s, \nu)$, respectively. When (s, τ, ν) represent cylindrical coordinates, the bow shock may be fitted, but it must be located on edge 3.

The mesh in each zone is defined by the transformation $T1 \cdot T2$, where $T1$: $(\xi, \eta, \zeta) \rightarrow (s, \tau, \nu)$ and $T2$ $(s, \tau, \nu) \rightarrow (x, y, z)$. T2 is given by:

$$\begin{aligned} x &= s \cos(\tau) \\ y &= s \sin(\tau) \qquad \text{cylindrical coordinates} \\ z &= \nu \end{aligned} \tag{20}$$

$$\begin{aligned} x &= s \\ y &= \tau \qquad \text{cartesian coordinates} \\ z &= \nu \end{aligned}$$

while T_1 is defined as:

$$\begin{aligned} s &= b(\tau', \zeta) + [c(\tau'', \zeta) - b(\tau', \zeta)]f(\xi) \\ \tau &= \sigma(s', \zeta) + [\Psi(s'', \zeta) - \sigma(s', \zeta)]g(\eta) \\ \nu &= \zeta \end{aligned} \tag{21}$$

where

$$\tau' = \tau_4(\zeta) + (\tau_1(\zeta) - \tau_4(\zeta))g(\eta)$$

$$\tau'' = \tau_3(\zeta) + (\tau_2(\zeta) - \tau_3(\zeta))g(\eta)$$

$$s' = s_4(\zeta) + (s_3(\zeta) - s_4(\zeta))f(\xi)$$

$$s'' = s_1(\zeta) + (s_2(\zeta) - s_1(\zeta))f(\xi)$$

and (s_i, τ_i), $i = 1, 2, 3, 4$ are the coordinates of the corners. Here f and g are mesh clustering functions with $f(0) = g(0) = 0$ and $f(1) = g(1) = 1$. The computational domain for each zone is bounded by $0 \leq \xi \leq 1$, $0 \leq \eta \leq 1$, and $\zeta \geq 0$.

In each crossflow plane, the metric quantities, ξ_x, ξ_y, ξ_z, η_x, η_y, η_z, must be evaluated at cell centers. These parameters are used in the predictor step and to compute the step size. This is accomplished analytically as follows:

$$\begin{aligned} \xi_x &= (\tau_\eta s_x - s_\eta \tau_x)/j \; ; \; \eta_x = (-\tau_\xi s_x + s_\xi \tau_x)/j \; ; \; \zeta_x = \nu_x \\ \xi_y &= (\tau_\eta s_y - s_\eta \tau_y)/j \; ; \; \eta_y = (-\tau_\xi s_y + s_\xi \tau_y)j \; ; \; \zeta_y = \nu_y \\ \xi_z &= (s_\eta \tau_\zeta - \tau_\eta s_\zeta)/j \; ; \; \eta_z = (\tau_\xi s_\zeta - s_\xi \tau_\zeta)/j \; ; \; \zeta_z = \nu_z \end{aligned} \tag{22}$$

where: $j = s_\xi \tau_\eta - s_\eta \tau_\xi$

The x, y, z derivatives of s, τ, ν are given in cylindrical and cartesian coordinates by:

$$\begin{aligned} &s_x = \cos(\tau), \; s_y = \sin(\tau), \; s_z = 0 \\ &\tau_y = \cos(\tau)/s, \; \tau_x = -\sin(\tau)/s, \; \tau_z = 0 \qquad \text{cylindrical coordinates} \\ &\nu_x = \nu_y = 0, \; \nu_z = 1 \end{aligned} \tag{23a}$$

$$\begin{aligned} &s_x = 1, \; s_y = s_z = 0 \\ &\tau_y = 1, \; \tau_x = \tau_z = 0 \qquad \text{cartesian coordinates} \\ &\nu_z = 1, \; \nu_x = \nu_y = 0 \end{aligned} \tag{23b}$$

The derivatives of s, τ, with respect to ξ, η, ζ, are evaluated analytically. The expressions for these quantities involve corner values of s_ρ and τ_ρ, which can be computed using the formulas given below:

$$\begin{aligned} s_{1_\zeta} &= (b_\nu + b_\tau \psi_\nu)/(1 - b_\tau \psi_s); \; \tau_{1_\zeta} = (\psi_\nu + \psi_s b_\nu)/(1 - b_\tau \psi_s) && \text{corner 1} \\ s_{2_\zeta} &= (c_\nu + c_\tau \psi_\nu)/(1 - c_\tau \psi_s); \; \tau_{2_\zeta} = (\psi_\nu + \psi_s c_\nu)/(1 - c_\tau \psi_s) && \text{corner 2} \end{aligned} \tag{24}$$

$$\begin{aligned} s_{3_\zeta} &= (c_\nu + c_\tau \sigma_\nu)/(1 - c_\tau \sigma_s) \; ; \; \tau_{3_\zeta} = (\sigma_\nu + \sigma_s c_\nu)/(1 - c_\tau \sigma_s) && \text{corner 3} \\ s_{4_\zeta} &= (b_\nu + b_\tau \sigma_\nu)/(1 - b_\tau \sigma_s) \; ; \; \tau_{4_\zeta} = (b_\nu + \sigma_s b_\nu)/(1 - b_\tau \sigma_s) && \text{corner 4} \end{aligned}$$

Using the corner values of s_ζ and τ_ζ, derivatives of s', s", τ' and τ'' can be computed as follows:

$$
\begin{aligned}
s'_\xi &= (s_3 - s_4)f'(\xi) \quad ; \quad s''_\xi = (s_2 - s_1)f'(\xi) \\
s'_\zeta &= s_{4_\zeta}\,\bar{f}(\xi) + s_{3_\zeta} f(\xi); \quad s''_\zeta = s_{1_\zeta}\,\bar{f}(\xi) + s_{2_\zeta} f(\xi) \\
s'_\eta &= 0 \quad ; \quad s''_\eta = 0 \\
\tau'_\xi &= 0 \quad ; \quad \tau''_\xi = 0 \\
\tau'_\zeta &= \tau_{4_\zeta}\,\bar{g}(\eta) + \tau_{1_\zeta} g(\eta) \; ; \quad \tau''_\zeta = \tau_{3_\zeta}\,\bar{g}(\eta) + \tau_{2_\zeta} g(\eta) \\
\tau'_\eta &= (\tau_1 - \tau_4)g'(\eta) \quad ; \quad \tau''_\eta = (\tau_2 - \tau_3)g'(\eta)
\end{aligned}
\tag{25}
$$

where:

$$
f'(\xi) = \frac{df(\xi)}{d\xi}\,, \quad g'(\xi) = \frac{dg(\xi)}{d\xi}\,, \quad \bar{f}(\xi) = 1-f(\xi), \quad \bar{g}(\xi) = 1-g(\xi)
$$

The general formulas for the transformation quantities then follow:

$$
\begin{aligned}
s_\xi &= (c-b)f'(\xi) \\
s_\eta &= b_\tau \tau'_\eta f(\xi) + c_\tau \tau''_\eta f(\xi) \\
s_\zeta &= (b_\tau \tau'_\zeta + b_\nu)\bar{f}(\xi) + (c_\tau \tau''_\zeta + c_\nu) f(\xi) \\
\tau_\xi &= \sigma_r s'_\zeta \bar{g}(\eta) + \psi_s s'_\zeta\, g(\eta) \\
\tau_\eta &= (\psi-\sigma)g'(\eta) \\
\tau_\zeta &= (\sigma_s s'_\tau + \sigma_\nu)\overline{g(\eta)} + (\psi_s s''_\tau + \psi_\nu)g(\eta)
\end{aligned}
\tag{26}
$$

Additional mesh-related information required by the Godunov procedure is the area of each cell in the crossflow plane (A_{ij}), and vectors normal ($\bar{n}$) to the sides of the control volume (see Figure 8). These quantities are computed as follows:

$$
A_{ij} = \frac{1}{2}\,|V_{64} \times V_{51}| \tag{27a}
$$

$$
\bar{n}_{i+1/2,j} = \frac{1}{2}\,(V_{24} \times V_{31}) \tag{27b}
$$

Here, $\bar{V}_{ij} = (x_i - x_j,\ y_i - y_j,\ z_i - z_j)$, where the subscripts refer to the corner numbers, which for cell (i,j) and edge (i + 1/2, j), are defined in Figure 8. If the edge corners are not in a plane, n lies in an area weighted average normal direction to the edge (see Reference 12). Note that the magnitude of the normal vector is the side area.

3.2 SECOND ORDER GODUNOV SCHEME

Using the notation and coordinates of Figure 8, control volume mass and momentum conservation equations are given by:

$$\overline{U}^{n+1}_{i,j} = \overline{U}^{n}_{i,j} - \overline{F}_{i+1/2,j} + \overline{F}_{i-1/2,j} - \overline{F}_{i,j+1/2} + \overline{F}_{i,j-1/2} \tag{28}$$

where:

$$\overline{U}^{n}_{i,j} = A^{n}_{i,j} \begin{bmatrix} \rho w \\ \rho w^2 + p \\ \rho w u \\ \rho w v \end{bmatrix}_{i,j} = \begin{bmatrix} u_1 \\ u_2 \\ u_3 \\ u_4 \end{bmatrix}_{i,j} \qquad F_{i+1/2,j} = \begin{bmatrix} \rho V \\ \rho w V + n_z p \\ \rho u V + n_x p \\ \rho v V + n_y p \end{bmatrix}_{i+1/2,j}$$

$$V = \bar{n}_{i+1/2,j}(u, v, w)_{i+1/2,j}$$

Here U is the flux in the z direction which passes through the shaded cell ends (see Figure 8) while the F's are the fluxes associated with the remaining cell edges. Eqs. (28) are closed using the constant total enthalpy condition and the perfect gas equation of state which yield the constraint:

$$\frac{p}{\rho}\frac{\gamma}{(\gamma-1)} + \frac{1}{2}(u^2 + v^2 + w^2) = H_o \tag{29}$$

In non-conservation form, Eqs. (28) becomes:

$$u_\zeta = \frac{-1}{w}\left[u_\xi \overline{U} + u_\eta \overline{V} + \frac{(\xi_x p_\xi + \eta_x p_\eta)}{\rho}\right]$$

$$v_\zeta = \frac{-1}{w}\left[v_\xi \overline{U} + v_\eta \overline{V} + \frac{(\xi_y p_\xi + \eta_y p_\eta)}{\rho}\right] \tag{30}$$

$$w_\zeta = \frac{1}{(w^2 - a^2)}\left[H_1 - wH_2 + P/\rho\right]$$

$$p_\zeta = \frac{1}{(w^2 - a^2)}\left[-\rho w H_1 + \rho a^2 H_2 - wP\right] - \xi_z p_\xi - \eta_z p_\eta$$

where:

$$\overline{U} = \xi_x u + \xi_y v + \xi_z w$$

$$\overline{V} = \eta_x u + \eta_y v + \eta_z w$$

$$P = u(\xi_x p_\xi + \eta_x p_\eta) + v(\xi_y p_\xi + \eta_y p_\eta)$$

$$H_1 = a^2\{\xi_x u_\xi + \xi_y v_\xi + \xi_z w_\xi + \eta_x u_\eta + \eta_y v_\eta + \eta_z w_\eta\}$$

$$H_2 = \bar{U} w_\xi + \bar{V} w_\eta$$

The solution to a supersonic flow field can be marched in the z direction using Eq. (28). The complete second order Godunov method evaluates the F fluxes and completes a marching step as follows:

1. Derivatives of p, ρ, u, v, w are computed using a limiter. To illustrate the limiter, consider the derivative which is calculated as follows:

$$\frac{\partial p}{\partial \xi}\Big|_{i,j} = \begin{cases} 0 & \text{if } (p_{i+1,j} - p_{i,j})(p_{i,j} - p_{i-1,j}) < 0 \\ \dfrac{(F)\min}{\Delta\xi}\left[\dfrac{|p_{i+1,j} - p_{i-1,j}|}{2},\ K|p_{i+1,j} - p_{i,j}|,\ K|p_{i,j} - p_{i+1,j}|\right] & \text{otherwise} \end{cases} \quad (31)$$

where: $F = \text{sign}(p_{i+1,j} - p_{i,j})$

Here K is an adjustable constant, which is normally set to unity at interior points.

2. The metrics ξ_x, ξ_y, ξ_z, are calculated at each cell center in the computation using Eqs. 22.

3. The step size, Δz, is determined from the (CFL) condition which is described below and discussed in Appendix A.

4. The predictor values, $\bar{p}$, $\bar{\rho}$, $\bar{u}$, $\bar{v}$, $\bar{w}$ are calculated at $z + \Delta z/2$ using the derivatives determined in step 1 and the metrics from step 2 applied to Eq. (30).

5. The coordinates of the control volume corners are determined from Eqs. (21), and the vectors normal to cell edges are computed using Eq. (27b).

6. Properties adjacent to cell edges at $z + \Delta z/2$ are calculated using the cell center predicted values from step 4 and the derivatives from step 1. This produces two sets of properties associated with each cell edge; one for each of the adjacent cells. For example, the two pressures on the lower edges of cell (i, j) in Figure 8 are:

$$\begin{matrix} p_{i,j} - \frac{1}{2}\frac{\partial p}{\partial \xi}\Big|_{i,j} & \text{from cell } (i, j) \\ p_{i-1,j} + \frac{1}{2}\frac{\partial p}{\partial \xi}\Big|_{i-1,j} & \text{from cell } (i-1, j) \end{matrix} \quad (32)$$

7. A Riemann problem is constructed at each cell edge using the two sets of properties determined in step 6. The two dimensions associated with the Riemann problem are defined by plane R which contains the cell edge normal vector and is aligned with the z axis. The two initial states consist of $(p, \ , v_n, w)$, at the two adjacent cells, where $v_n = (n_x, n_y) \cdot (u, v)/|(n_x, n_y)|$. Also computed for each initial state is $v_t = (-n_y, n_x) \cdot (u, v)/|(n_x, n_y)|$ which is the velocity component tangent to the cell edge trace in the $z = z^n$ plane.

8. The Riemann problem associated with each cell edge is solved using the techniques described in Section 2.2.

9. The angular orientation of the cell edge in plane R is calculated with respect to edge (i+1/2,j). This orientation is:

$$\theta = \tan^{-1}\left[- \frac{n_{z_{i+1/2,j}}}{(n^2_{x_{i+1/2,j}} + n^2_{y_{i+1/2,j}})^{1/2}}\right] \tag{33}$$

10. Cell edge properties are constructed using the Riemann solution along direction θ, and by specifying v_t. In terms of the properties provided by the Riemann solution, p_θ, ρ_θ, q_θ, δ_θ, the cell edge properties, denoted by a subscript e, are given by:

$$\begin{aligned} p_e &= p_\theta \\ \rho_e &= \rho_\theta \\ u_e &= (q_\theta \sin\delta n_x - v_t n_y)/|n_x, n_y| \\ v_e &= (q_\theta \sin\delta n_y + v_t n_x)/|n_x, n_y| \\ w_e &= q_\theta \cos\delta \end{aligned} \tag{34}$$

In the above, q and δ are the velocity magnitude and flow direction. v_t is selected by noting the relative sizes of θ and δ_f, the Riemann slip line direction. The following algorithm is used:

$$v_{t_{i+1/2,j}} = \begin{cases} v_{t_{i+1,j}} & \text{if } \theta > \delta_f \\ v_{t_{i,j}} & \text{if } \theta < \delta_f \end{cases} \tag{35}$$

11. Using p_e, ρ_e, u_e, v_e, w_e, for each of the four cell edges, fluxes are evaluated and the flow field is advanced using Eqs. (28).

12. The computational step is completed by calculating cell end areas at $z + \Delta z$ using Eqs. (27a) and decoding to determine the primitive variables as follows:

$$u_{i,j} = (u_3/u_1)_{i,j}$$

$$v_{i,j} = (u_4/u_1)_{i,j}$$

$$w_{i,j} = \frac{\gamma}{(\gamma+1)} \left[\frac{u_2}{u_1}\right]_{i,j} \left[\left|1 - \frac{\gamma^2-1}{\gamma^2} x\right|\right]^{1/2} \qquad (36)$$

where: $x = [(2H_o u_1^2 - u_3^2 - u_4^2)/u_2^2]_{i,j}$

$$p_{i,j} = (u_2 - w u_1)_{i,j}/A_{i,j}$$

$$\rho_{i,j} = u_{1_{i,j}}/(w_{i,j} A_{i,j})$$

In the above, p is positive provided that $x > 1$.

The step size $\Delta\zeta$ is chosen using the CFL condition, which requires that the following condition be satisfied at every point:

$$\Delta\zeta = \frac{(w^2 - a^2)\Delta\eta}{\delta c_1 + c_2 + [a^2\{c_3\delta^2 + c_4 + c_5\delta\}]^{1/2}} \qquad (37)$$

where: $c_1 = |a^2\xi_z - w\bar{U}|$

$$c_2 = |a^2\eta_z - w\bar{V}|$$

$$c_3 = (w\xi_z - \bar{U})^2 + (w^2 - a^2)(\xi_x^2 + \xi_y^2)$$

$$c_4 = (w\eta_z - \bar{V})^2 + (w^2 - a^2)(\eta_x^2 + \eta_y^2)$$

$$c_5 = 2|(w\xi_z - \bar{U})(w\eta_z - \bar{V}) + (w^2 - a^2)(\eta_x\xi_x + \eta_y\xi_y)|$$

$$\delta = (\Delta\eta/\Delta\xi)$$

The second order Godunov scheme is modified when the approximate Riemann problem is used. Steps 7 and 8 are removed while the fluxes, determined in steps 10 and 11, are computed by the three-dimensional version of Eq. (18):

$$\overline{F^*} = \frac{a^- a^+ (\overline{U^+} - \overline{U^-}) \left| (n_x, n_y) \right| + a^+ \overline{F^-} - a^- \overline{F^+}}{(a^+ - a^-)} \tag{38}$$

Here, $\overline{F^+}$, $\overline{F^-}$, F* are the total flux through the control volume edges (i.e., the fluxes of Eq. 18 multiplied by the edge areas). However, U^+, U^- are still the end-area flux per unit area.

3.3 BOUNDARY CONDITIONS

Five types of boundary conditions can be applied along zone edges. These are listed in Table 1 along with the edges on which each can occur.

The INTERIOR boundary condition allows interior cells of adjacent zones to interface. The second order Godunov scheme outlined in the previous section is applied. Here it is presumed that the mesh is continuous across zone boundaries. Failure to use a continuous mesh will result in loss of second order accuracy.

The SYMMETRY boundary condition permits the modeling of symmetry planes and consists of a second order Godunov scheme operating on an automatically constructed mirror image state.

Ambient condidtions are automatically applied to boundary cells at which the FREESTREAM condition is invoked. This procedure advances the solution as if a surface were adjacent to the boundary cell. However, at the end of the computational step, computed properties are over-written by ambient ones.

The SURFACE boundary conditions allow a surface to be simulated. At cells adjacent to a surface, the second order Godunov scheme must be modified. The derivatives normal to the surface are calculated using a one-sided difference. Also, the flux passing through the cell edge adjacent to the surface must be computed to reflect the tangent flow boundary condition.

The slopes normal to the surface are determined using the following one-sided difference limiter:

$$\frac{\partial p}{\partial \xi} = \begin{cases} 0 \quad \text{if } (p_{i+1,j} - p_{i,j})(p_{i,j} - p_{i-1,j}) < 0 \\ \\ \qquad\qquad \text{otherwise} \\ \\ \dfrac{F'MIN}{\Delta\xi} \left[-1.5p_{1,j} + 2p_{2,j} - .5p_{3,j},\ K'(p_{3,j} - p_{2,j}),\right. \\ \\ \left. K'(p_{2,j} - p_{1,j}) \right] \end{cases} \tag{39}$$

where: $F' = \text{sign}(p_{3,j} - p_{2,j})$

In smooth regions of the flow field, K' is set to 2 while near fin leading edge, a K' value of zero is used.

The flux on the cell edge adjacent to the wall is evaluated using the procedure:

1. Following the predictor step, properties at cell edges adjacent to the walls are computed by extrapolating predicted p, ρ, u, v, w to the wall using the cell slope normal to the wall.

2. The velocity vector determined in step 1 is turned through either a shock or expansion in plane R. The appropriate turn aligns the velocity with the wall.

3. The wall is a steamline and the flux at the wall reduces to:

$$F_{1/2,j} = \begin{bmatrix} 0 \\ n_z p \\ n_x p \\ n_y p \end{bmatrix}$$

The wall flux is evaluated using the pressure determined in step 2.

On edges 2 and 4, fin surfaces may form or disappear as the solution is marched down the length of the missile. Here it is possible for only part of a cell to be covered by a surface, as is illustrated in Figure 9. Such cell edges are divided into an interior and a surface part. Separate flux values are constructed for each and summed to determine the total flux passing through the cell edge. The procedure for calculating the interior and surface fluxes follows from the surface and interior flux algorithms discussed above. To implement these schemes, it is necessary to construct vectors normal to the interior and surface portion of the cell edges. The magnitude of the surface normals is equal to the areas of the interior and surface portions of the cell edge, respectively. An estimate of the areas of the surface and interior portions of the cell edge is determined by dividing the cell edge into six sections as shown in Figure 9. The total and surface areas are calculated from:

$$A_{tot} = \sum_{i=1}^{6} (R_{O_i} - R_{I_i})\Delta\ell_i \qquad \text{(total area)} \tag{40}$$

$$A_{surf} = \sum_{i=1}^{6} \max[(R_{T_i} - R_{B_i}), 0]\Delta\ell_i \qquad \text{(surface area)}$$

where: $\Delta\ell_1 = \Delta\ell_6 = \Delta z/12$, $\Delta\ell_i = \Delta z/6$, $i = 2, 3, 4, 5$

$$R_{o_i} = r_1 + \frac{\sum_{j=1}^{i} \Delta\ell_j}{(z_2 - z_1)} (r_2 - r_1)$$

$$R_{I_i} = r_4 + \frac{\sum_{j=1}^{i} \Delta\ell_j}{(z_2 - z_1)} (r_3 - r_4)$$

$$R_{T_i} = \min(p_{e_o}(z), R_{o_i})$$

$$R_{B_i} = \max(p_{e_i}(z), R_{I_i})$$

$p_{e_o}(z)$ = outer fin tip radial location

$p_{e_i}(z)$ = inner fin tip radial location

r_i = radius at corner i (see Figure 9 for numbering convention).

The vectors normal to the surface, $\bar{n}_{surf}$, and interior, $\bar{n}_I$, parts of the cell edge then follow from:

$$\bar{n}_{surf} = \frac{\bar{n}'}{|\bar{n}'|} \frac{A_{surf}}{A_{tot}} |\bar{n}| \tag{41a}$$

$$\bar{n}_I = \bar{n} - \bar{n}_{surf} \tag{41b}$$

where:

edge 2

$$\bar{n}'_{surf} = \begin{cases} [-\sin\tau/s + \Psi_\tau \cos\tau, \ \cos\tau/s - \sin\tau\Psi_s, \ \Psi_\nu] & \text{cylindrical} \\ [-\Psi_s, \ 1 - \Psi_\nu] & \text{cartesian} \end{cases} \tag{42a}$$

edge 4

$$\bar{n}'_{surf} = \begin{cases} [-\sin\tau/s + \sigma_\tau \cos\tau,\ \cos\tau/s - \sin\tau_s,\ \sigma_\nu] & \text{cylindrical} \\ [-\sigma_s,\ 1,\ -\sigma_\nu] & \text{cartesian} \end{cases} \quad (42b)$$

Here Ψ and σ are evaluated at $[z_J, \frac{1}{2}(R_{T_J} + R_{B_J})]$ where J is first segment for which $\max(R_{T_J} - R_{B_J}, 0) > \varepsilon$ and $R_{o_J} - R_{I_J} - R_{T_J} + R_{B_J} > \varepsilon$, where ε is a small number.

The geometry of edge 3 can be computed to fit the domain of dependence of the solution when cylindrical coordinates are used. To invoke this procedure, the SHOCK boundary conditions are applied. The geometry of edge 3 is determined using the information contained within the solution of the Riemann Problem constructed on plane R. The two initial states for this problem are the free-stream and the abutting cell edge properties. The cell edge properties are obtained by extrapolating the center properties to the edge using differences normal to edge 3. The Riemann problem solution features a direction, θ_s, which separates the free-stream conditions from other states. This angle marks the domain of dependence of the numerical solution in plane R. Since plane R contains the cell edge normal, $\bar{n}$, the vector (n_x, n_y) is also in R. A vector directed along the θ_s direction is thus:

$$\bar{n}_s = \frac{1}{(n_x^2+n_y^2)^{1/2}} (n_x \underline{i} + n_y \underline{j}) - \tan\theta_s \underline{k} \quad (43)$$

Transforming to polar coordinates yields:

$$\bar{n}_s = \frac{1}{(n_x^2+n_y^2)^{1/2}} [(n_x\cos\phi + n_y\sin\phi)\bar{e}_r + (-\sin\phi n_x + \cos\phi n_y)\bar{e}_\phi] - \tan\theta_s \bar{e}_z \quad (44)$$

Noting that:

$$\bar{n}_s = \bar{e}_r - \frac{c_\phi}{c}\bar{e}_\phi - c_z\bar{e}_z \quad (45)$$

and comparing to the above yields:

$$c_z = \frac{\tan\theta_s (n_x^2 + n_y^2)^{1/2}}{[n_x\cos\phi + n_y\sin\phi]} \quad (46)$$

The procedure for computing the geometry of edge 3 is as follows:

Following the First Step of Main Algorithm

1. Compute c_z using Eq. (46) evaluated with n_x and n_y from the previous step. Cell edge properties are based on the cell center properties of the previous step, and the differences from step 1 of the second order Godunov algorithm.

Following the Predictor (Step 4 of Main Algorithm)

2. Re-evaluate c_z from Eq. (46) using predictor properties.

3. Advance the shock location using the c_z value determined in step 2 by means of:

$$c^{n+1} = c^n + (c_z + c_\phi \phi_\zeta)\Delta z \tag{47}$$

4. Update c_ϕ values using a central difference.

The algorithm used to advance the cell adjacent to the edge of the domain of dependence is altered in two respects. The derivatives in a direction normal to the edge 3 are computed in a manner analogous to that of Eq. 39, with K' = 2. The flux passing through the cell edge adjacent to the free stream is determined by a Riemann problem featuring free-stream properties and abutting cell edge properties as the two initial states.

3.4 SEPARATION MODELING

At incidences greater than a few degrees, the viscous flow about a missile body will separate and roll up to form leeside vortices. Inviscid calculations instead feature a strong crossflow shock which may generate sufficient vorticity to form leeside vortices. However, the strength of these vortices is much smaller than that of measured vortices. Also, the predicted inviscid pressure distribution differs markedly from the measured one. Several different methods have been proposed to model viscous crossflow separation.[1,13] The first of these alters the surface velocity direction near the estimated separation line, which is determined empirically. The second method limits the crossflow velocity to a certain maximum value. Both techniques destroy the crossflow shock and produce strong leeside vortices. However, modeling the separation line, which is the most physically realistic procedure, yields erratic pressure values near the separation line.

The ZEUS code implements the crossflow limiting approach. The crossflow plane velocity, $u^2 + v^2$, prior to decoding, is reduced to the following maximum Mach number:

$$M_{c_R} = (\alpha)^{1/2}(r/b)^2 \tag{48}$$

Here b is the local body radius, α is the angle of attack and r is the radial coordinate. The decode procedure, applied after the limiting process, enforces the correct stagnation enthalpy constraint. The above procedure has only been applied to turbulent flow, hence the absence of a Reynolds number dependency.

SECTION 4

RESULTS

The second order Godunov method has been applied to body alone as well as winged configurations. In all cases the missile nose was taken as sharp and the initial data plane was defined a short distance from the nose tip using the approximate conical flow field generator of Reference 9. The solution was advanced at 90% of the CFL step size and it was not necessary to apply either special differencing or artificial viscosity. The constant K in the limiter Eq. 31 was set to unity. Along edges 1 and 3, K' of Eq. 39 was set at 2, while on edges 2 and 4 it was set to 0. All of the results shown employ the approximate Riemann solver of Section 2.2. These results are nearly identical to those obtained using the approximate Riemann problem of Section 2.3.

Figures 10 and 11 illustrate the calculated surface pressure and crossflow plane velocities on a tangent ogive at a station 6.5 calibers from the nose tip. Both clipped and unclipped results are shown along with the measured surface pressure distribution.[14] Application of clipping destroys the crossflow shock, introduces a large leeside vortex, and brings the calculated leeside surface pressure into better agreement with experiment. On the windward side, the unclipped surface pressure results are closer to experiment.

Calculated surface pressures are shown in Figure 12 for a cruciform delta configuration in the plus roll orientation. Experimental data are from Reference 15 and were measured at a Mach number of 3.7, an incidence of 7.8°, and Reynolds number based on diameter of $1.8(10^5)$. For these conditions, attached shocks or expansions occurred at the fin leading edges. The calculation was started near the nose tip using a (18x24) mesh and run to a position slightly forward of the wing. The final section containing the fins extended from z = 80 to 102 and was run using a (36x36) mesh. The calculated surface pressure agrees well with experiment over most of the fin surface. The crossflow velocity vectors and pressure contours at an axial station near the fin mid-cord are given in Figures 13. Shocks can be seen attached to the fin edges.

Calculations have been performed on the two swept wing configurations shown in Figure 14. These bodies were tested at an incidence of 6° and Mach numbers of 2.5 and 4.5.[16] An (18x18) mesh was applied forward of the wing and a (36x36) mesh was used for the remainder of the body. Calculated and measured wing surface pressures are shown in Figure 14 and agree well in most cases. However, near the wing leading edge, computed values are larger than measured ones. Figure 15 provides measured and calculated surface pressure on the windward side and leeward side of the body. Calculated surface pressures generally agree well with experiment; however, discrepancies occur on the aft end of the body at Mach 4.5. On the windward side, the pressure rise due to

the presence of the wings is computed to occur downstream of the measured one, while on the leeside, predicted pressures exceed experimental values. However, these calculated results are in excellent agreement with those computed in Reference 17 and thus, these discrepancies are likely due to viscous effects. The crossflow pressure contours are shown in Figure 16 at an axial station upstream of the wing tip at Mach 2.5 and 4.5 for the thick wing case. A detached shock is visible below both wings and at the higher Mach number it is positioned closer to the wing surface. This produces the strong wing surface pressure gradients which are visible at this Mach number in Figure 14. At Mach 4.5, the Mach number normal to the leading edge is supersonic, but it is not large enough to produce an attached shock which could turn flow onto the plane of the lower wing surface.

The wing-body-tail configuration of Reference 18 is shown in Figure 17. It features a nighly swept wing with subsonic leading edge normal Mach number. A (36x36) mesh is applied over the complete model and both a deflected and undeflected horizontal tail configuration are considered. The computed normal force coefficient and center of pressure are given in Figure 17, with and without fin deflection, and agree well with experiment. The computed crossflow field at axial stations near the wing trailing edge and the middle of the tail are shown in Figure 18. Figure 19 features a contour plot of total pressure loss at these same axial stations.

SECTION 5

CONCLUDING COMMENTS

A second order Godunov method for tactical missiles in supersonic flow has been developed and applied to several different configurations. This scheme uses a multiple zone approach to generate a grid for finned tactical missile shapes. It is cast in a finite volume framework and fits the bow shock using the information contained in the Riemann problem. Results have been applied to several different missiles, with and without fins, and satisfactory agreement has been obtained with measurement. It was not necessary in any of these cases to use special procedures or artificial viscosity.

The merits of the second order Godunov scheme can be illustrated by comparing it to the MacCormack finite difference methods of References 1 and 2 (i.e., the SWINT and MUSE codes). All of these methods use a similar multiple zone mesh and calculations have been carried out on many of the shapes presented in this report. The principal advantage of the Godunov scheme discussed in this report is robustness. This allows complicated cases to be computed without user intervention or the application of special procedures. For example, computation of the wing-body-tail configuration shown in Figure 17, using the methods of References 1 or 2 requires fine tuning of the artificial viscosity level as well as careful selection of the fin differencing options. The second order Godunov method handled this configuration without user intervention or the application of special procedures. In the case of a tangent ogive at incidence (e.g., Figure 10), as the mesh is refined, the MacCormack schemes will fail unless artificial viscosity is added. The Godunov scheme sharply resolves the crossflow shock using a fine mesh and needs no special attention.

A disadvantage of the Godunov method is its computational cost which is on the order of 50% greater than the MacCormack methods. This problem can be reduced by using the approximate Riemann problem. Computations applying the approximate Riemann problem are 30% faster than those completed with the full problem, while the results are nearly identical to those achieved with the complete Riemann problem.

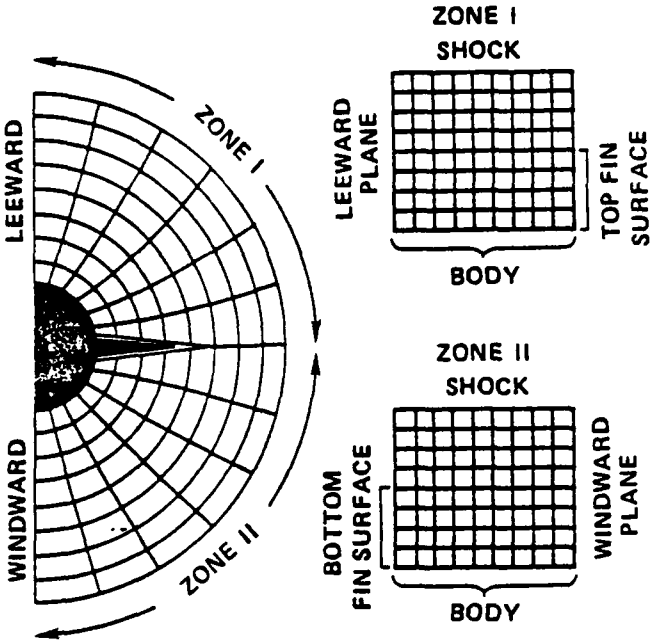

FIGURE 1. MULTIPLE ZONE MESH

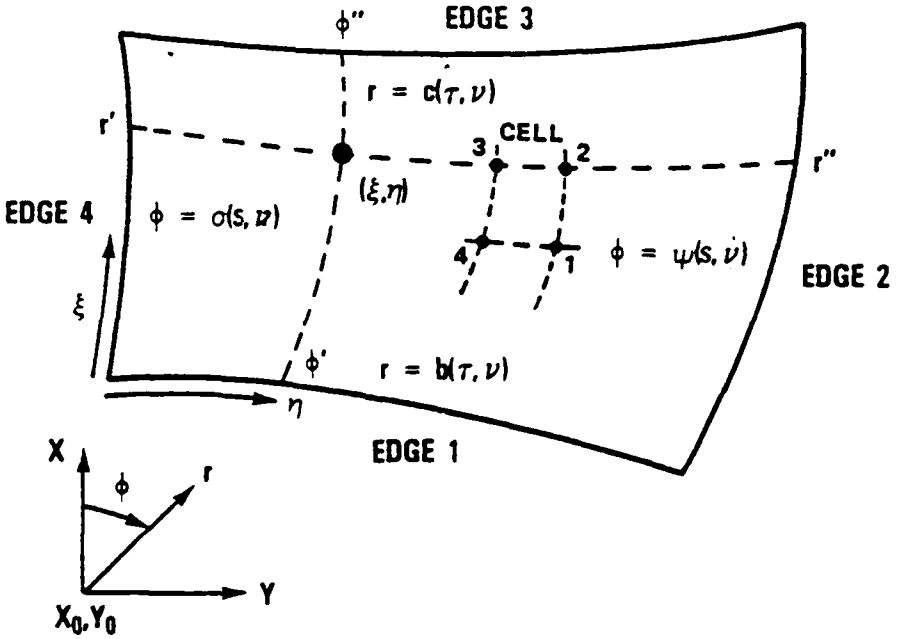

FIGURE 2. GENERALIZED QUADRILATERAL ZONE STRUCTURE

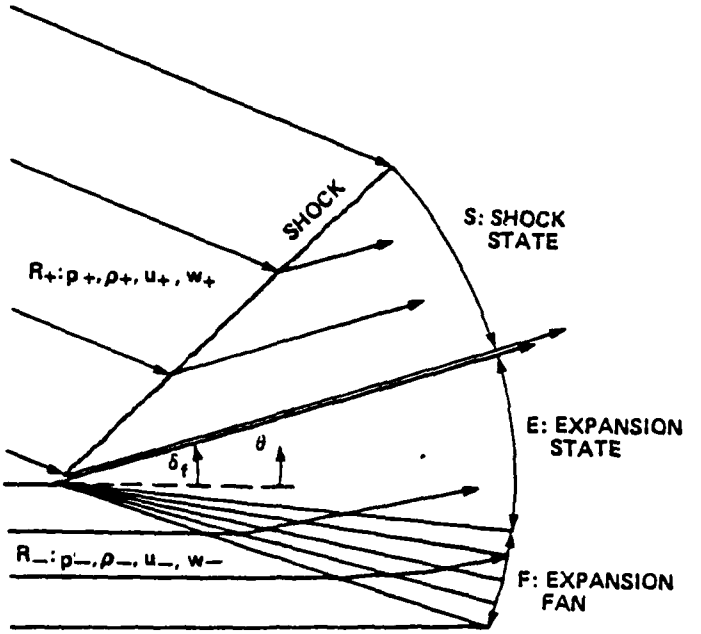

FIGURE 3. THE SUPERSONIC RIEMANN PROBLEM

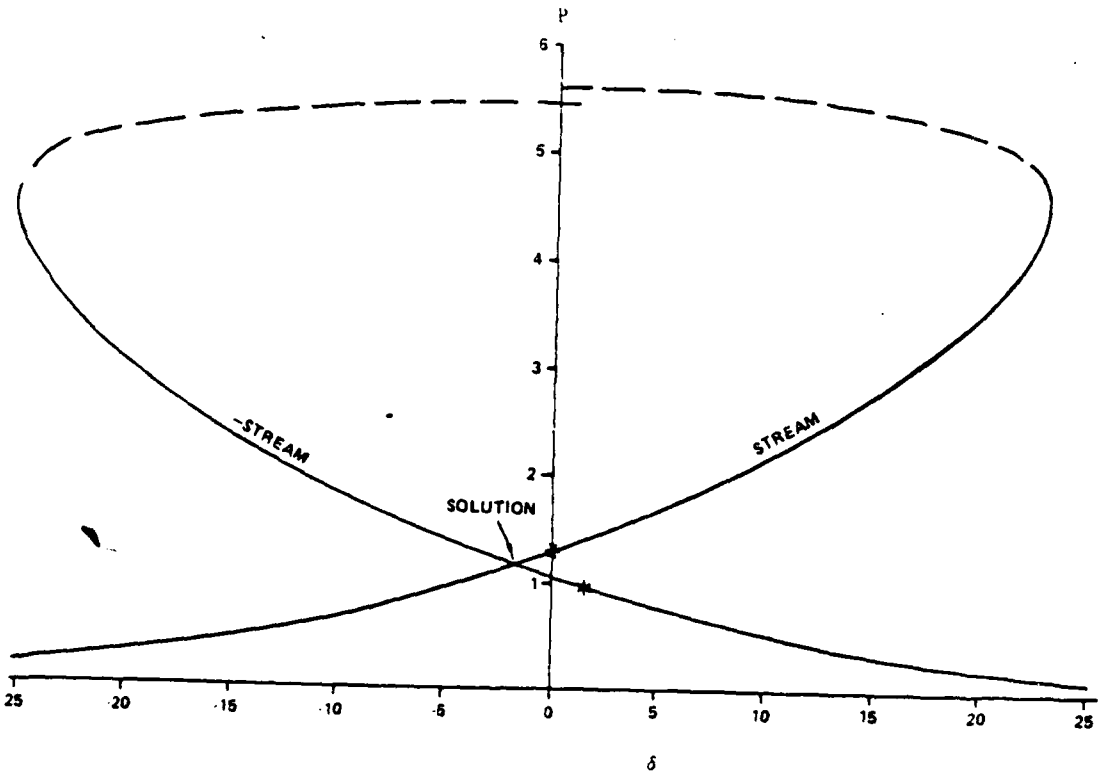

FIGURE 4. RIEMANN PROBLEM (P -δ) CURVE

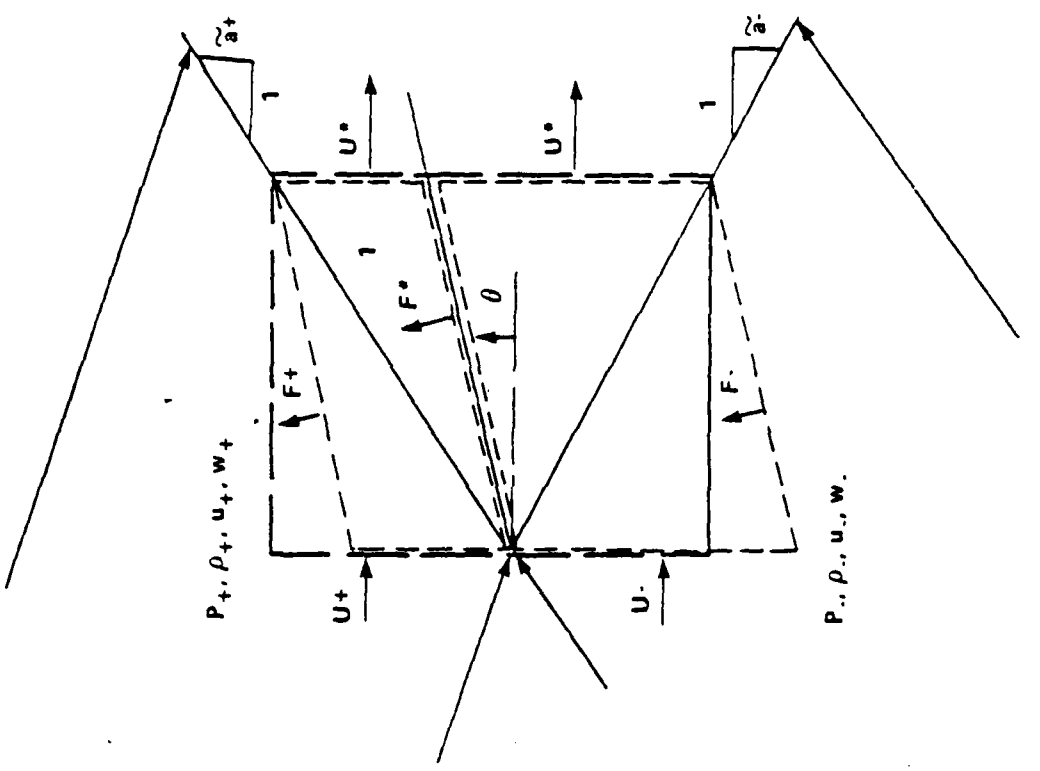

FIGURE 6. APPROXIMATE RIEMANN PROBLEM

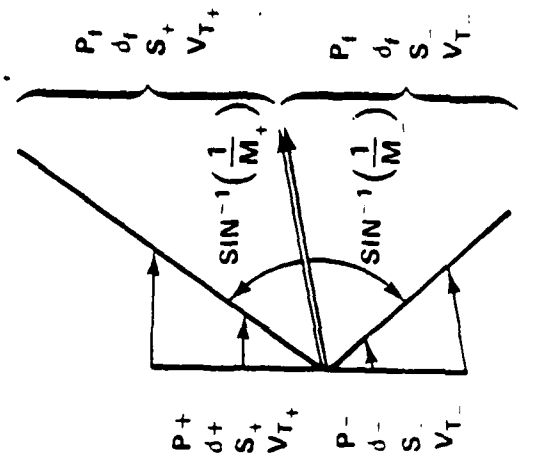

FIGURE 5. LINEARIZED RIEMANN PROBLEM

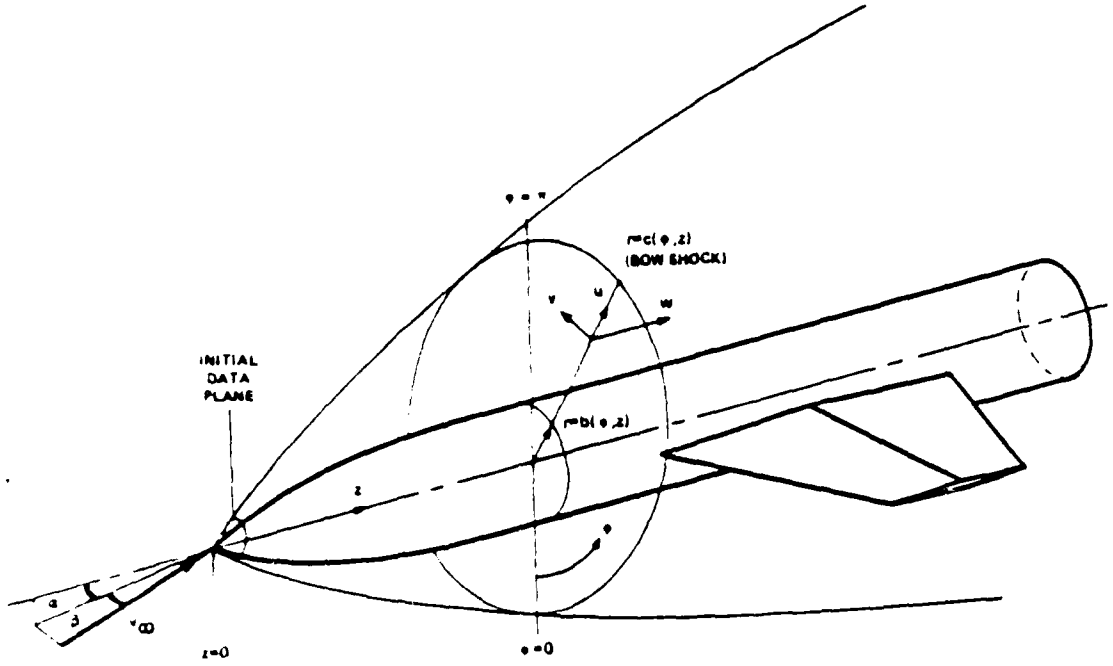

FIGURE 7. CARTESIAN AND CYLINDRICAL COORDINATE SYSTEM

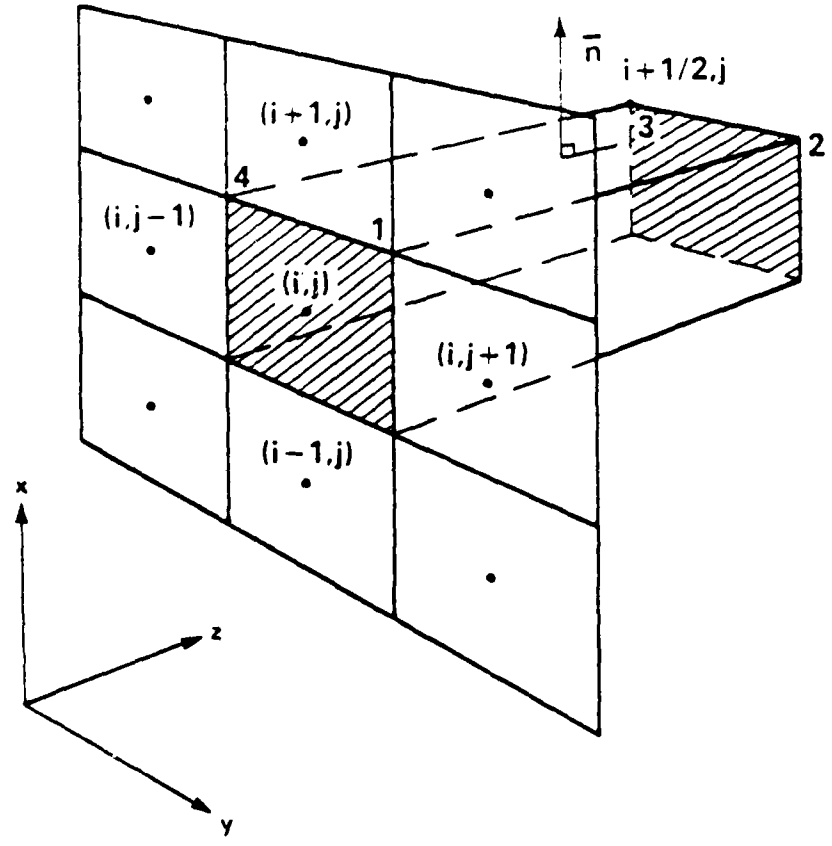

FIGURE 8. CONTROL VOLUME NOMENCLATURE

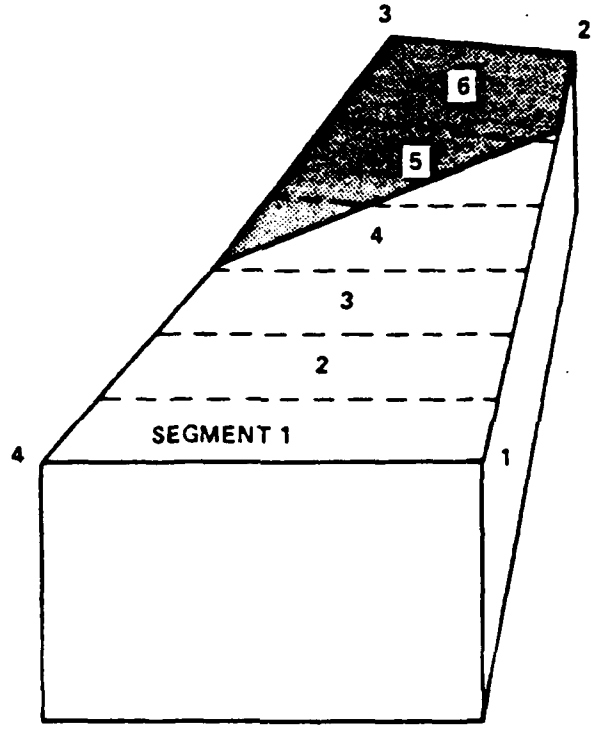

FIGURE 9. CELL PARTIALLY COVERED BY A SURFACE

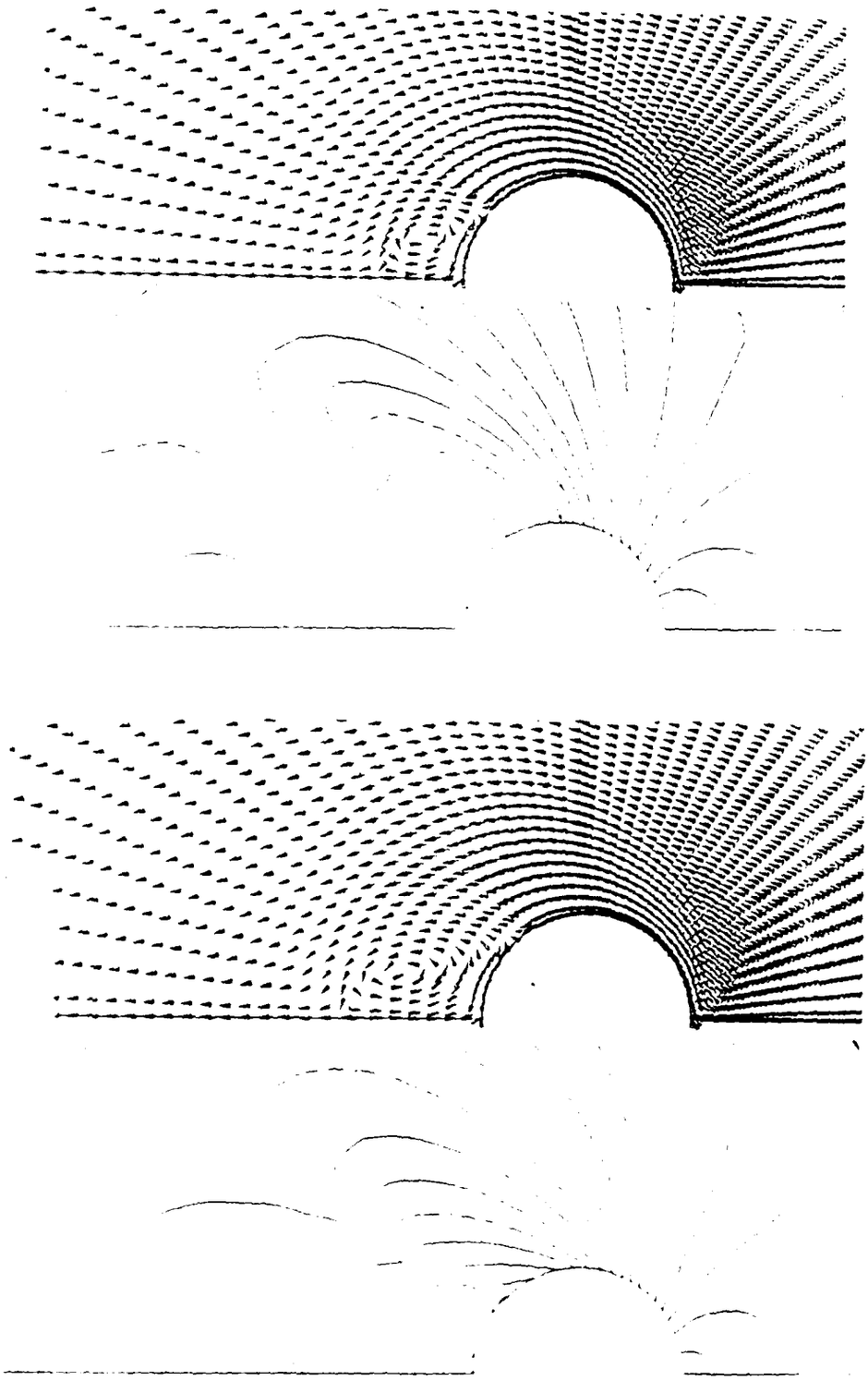

(B) WITH SEPARATION

(A) WITHOUT SEPARATION

FIGURE 10. COMPUTED CROSSFLOW FIELD ON A TANGENT OGIVE

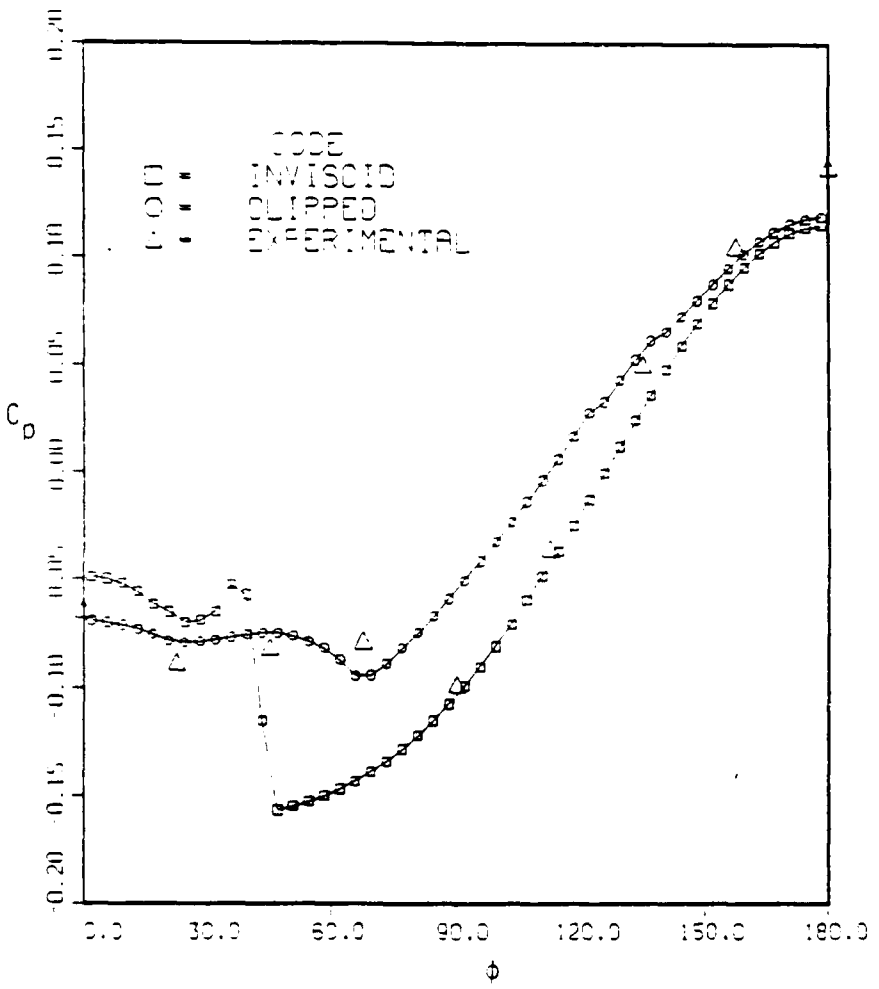

FIGURE 11. SURFACE PRESSURE ON A TANGENT OGIVE

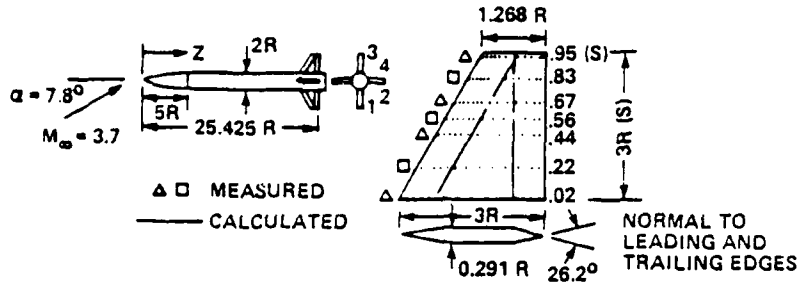

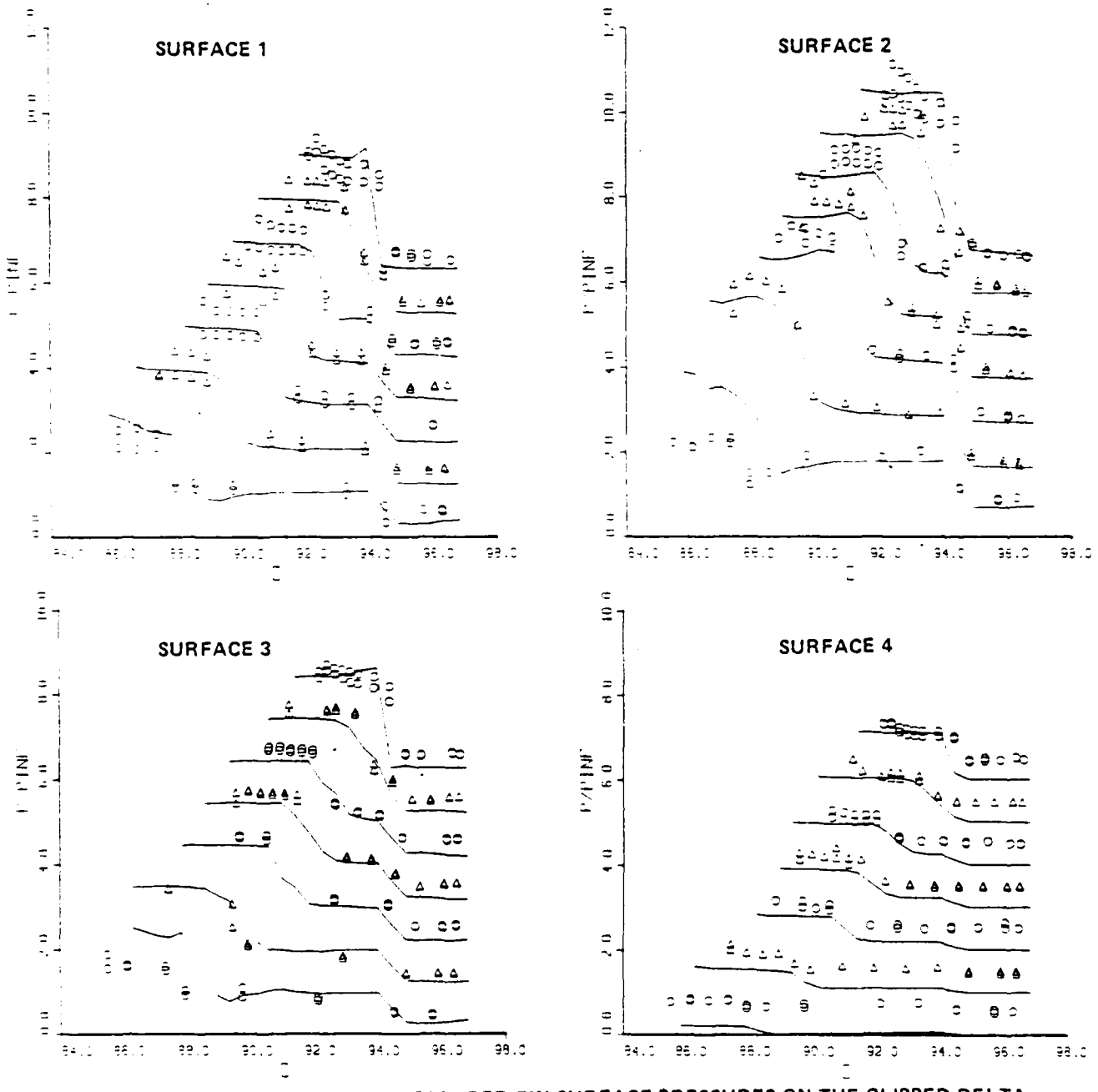

FIGURE 12. CALCULATED AND MEASURED FIN SURFACE PRESSURES ON THE CLIPPED DELTA WING CONFIGURATION OF REFERENCE 15. (SYMBOLS ARE MEASURED AND LINES ARE COMPUTED RESULTS. REFERENCE ZERO IS SHIFTED BY 1 FOR EACH SUCCESSIVE CURVE.)

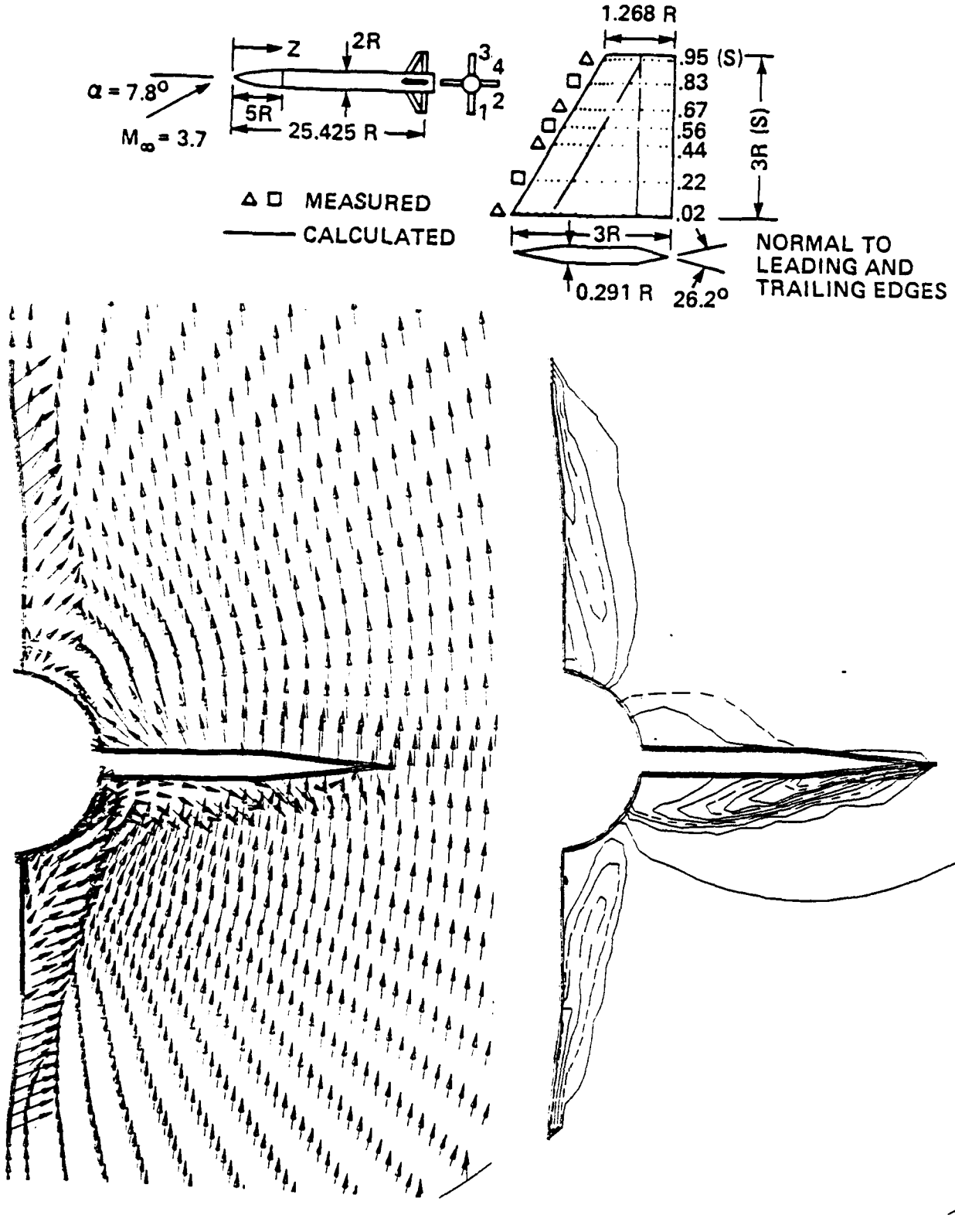

FIGURE 13. COMPUTED CROSSFLOW VELOCITIES AND PRESSURE CONTOURS AT STATION Z = 24.5R

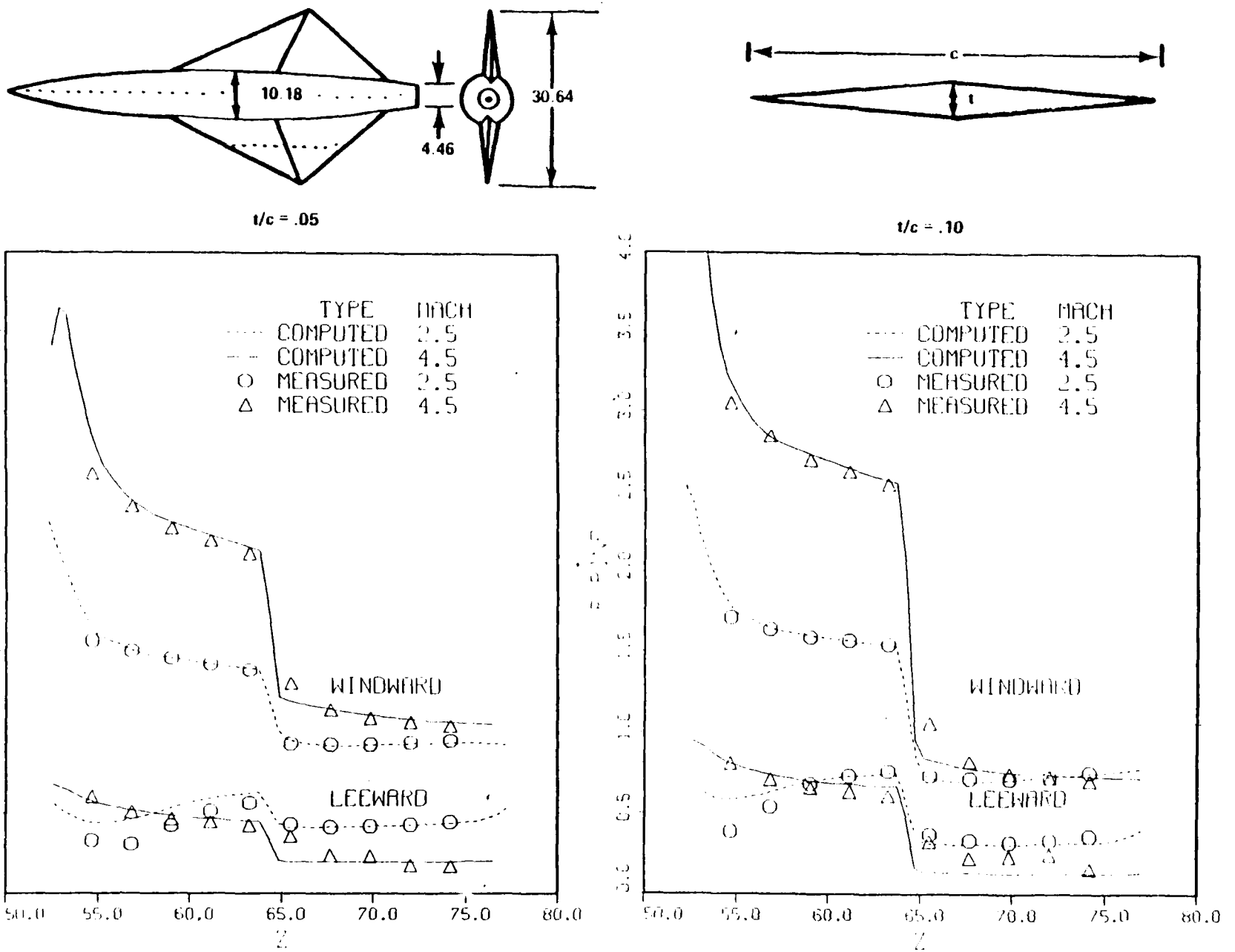

FIGURE 14. CALCULATED AND MEASURED WING SURFACE PRESSURES ON THE SWEPT WING MODEL OF REFERENCE 16 AT $\alpha = 6^{o}$

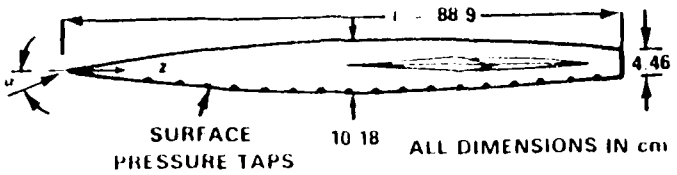

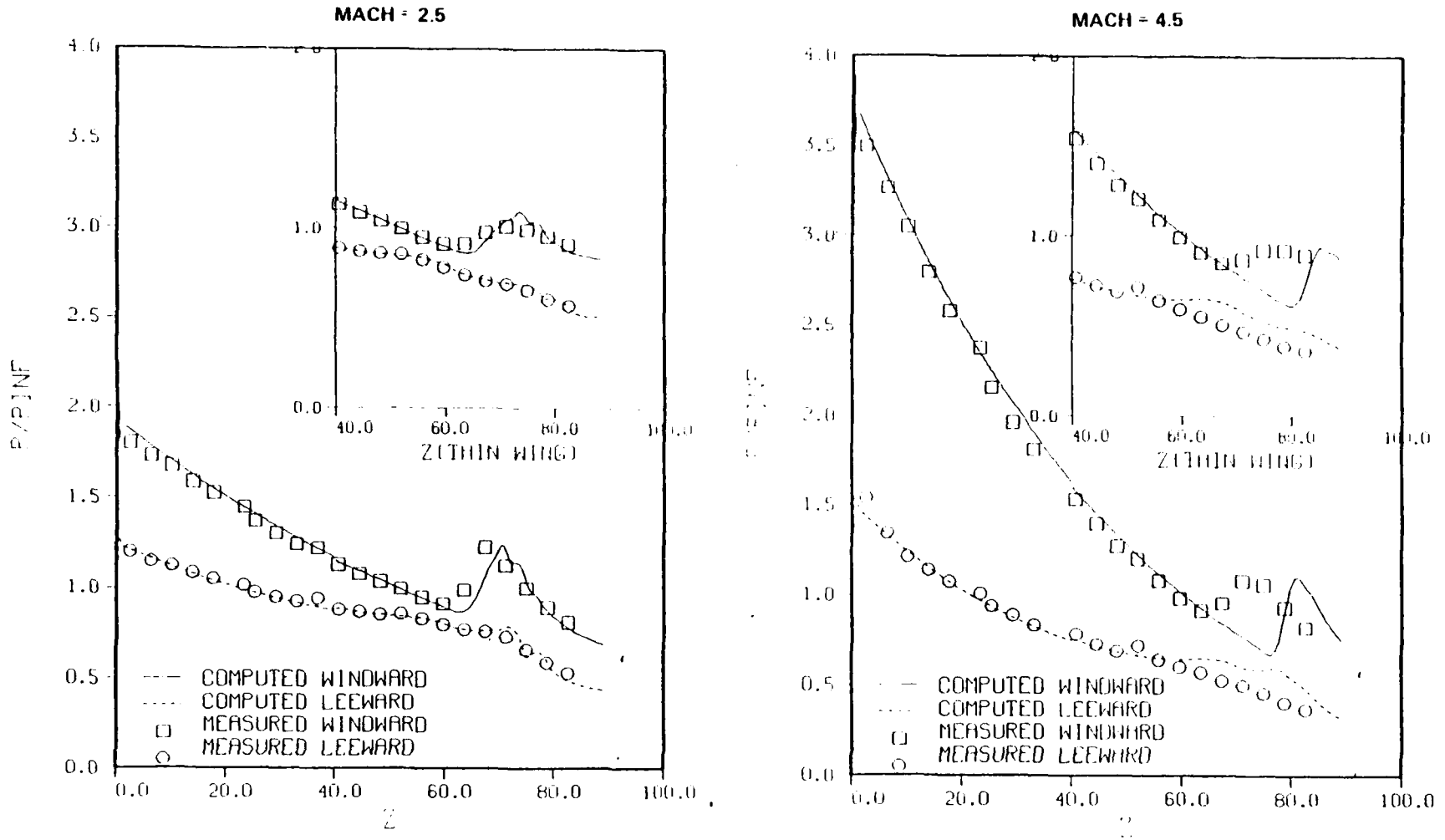

FIGURE 15. CALCULATED AND MEASURED BODY PRESSURES ON THE SWEPT WING MODEL OF REFERENCE 16 AT $\alpha = 6^{o}$

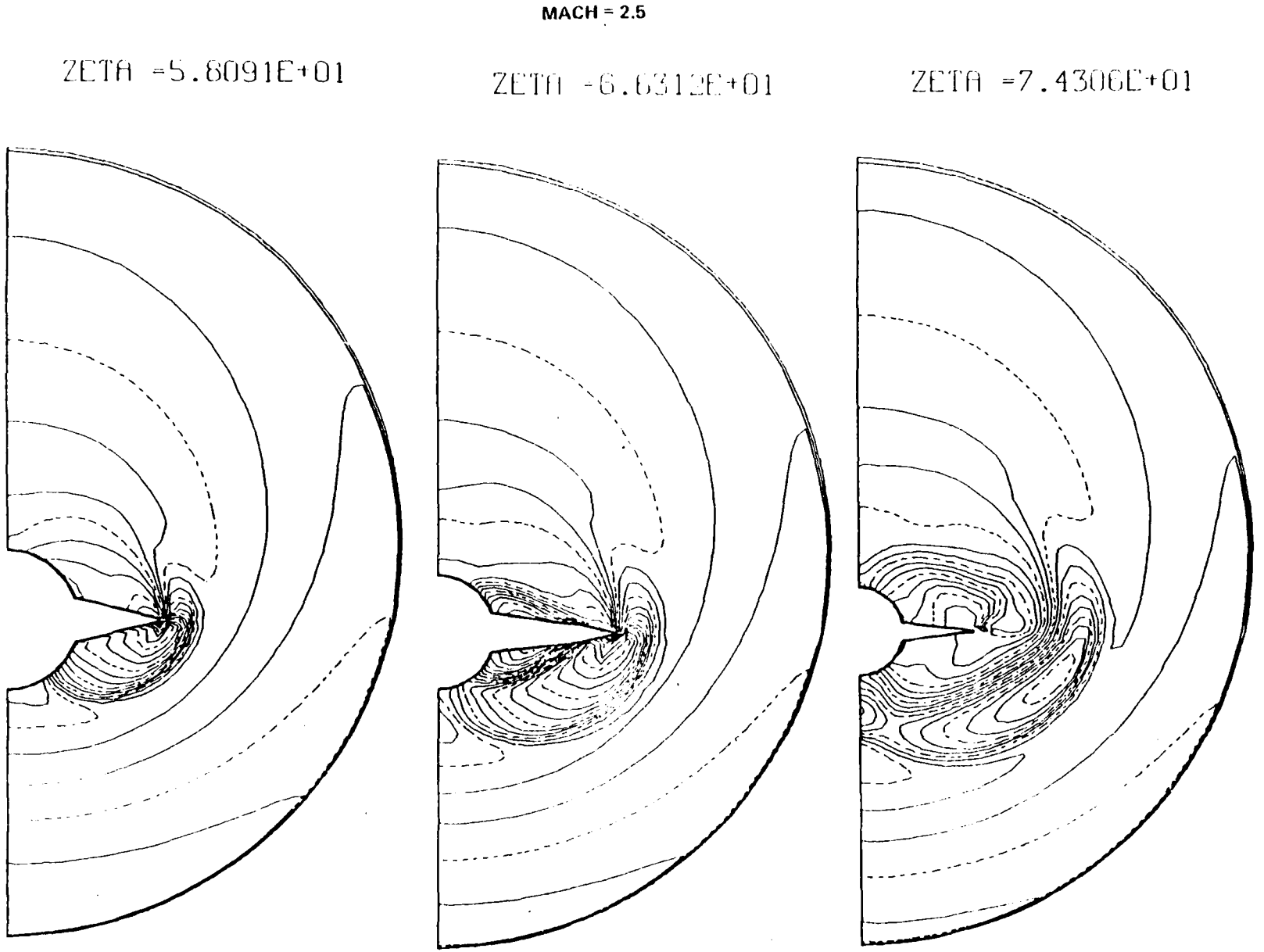

FIGURE 16. COMPUTED PRESSURE CONTOURS ON THE MODEL OF FIGURE 14

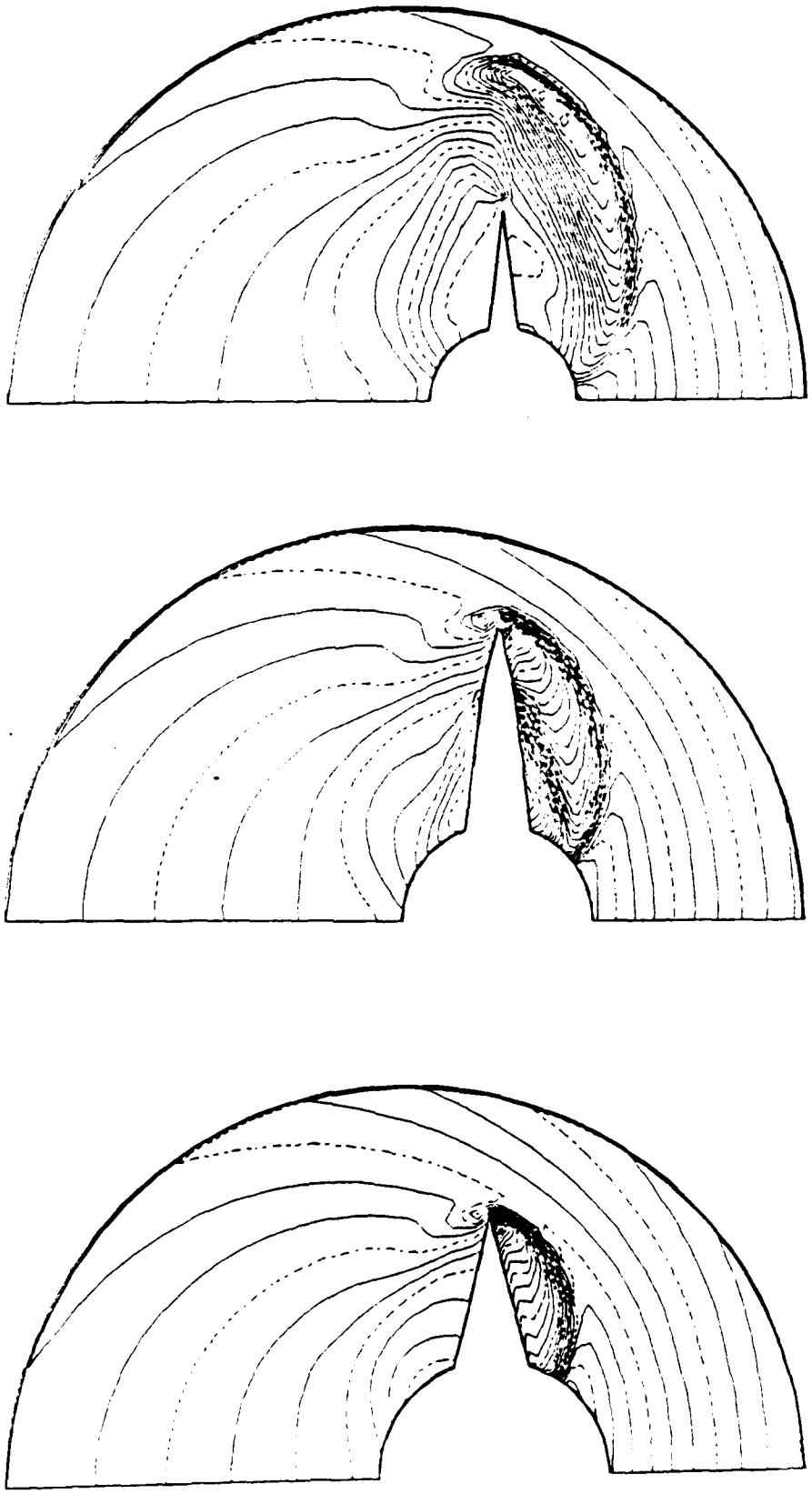

FIGURE 16. (CONTINUED)

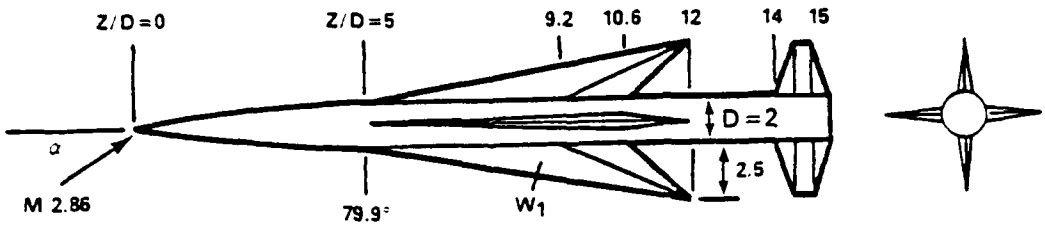

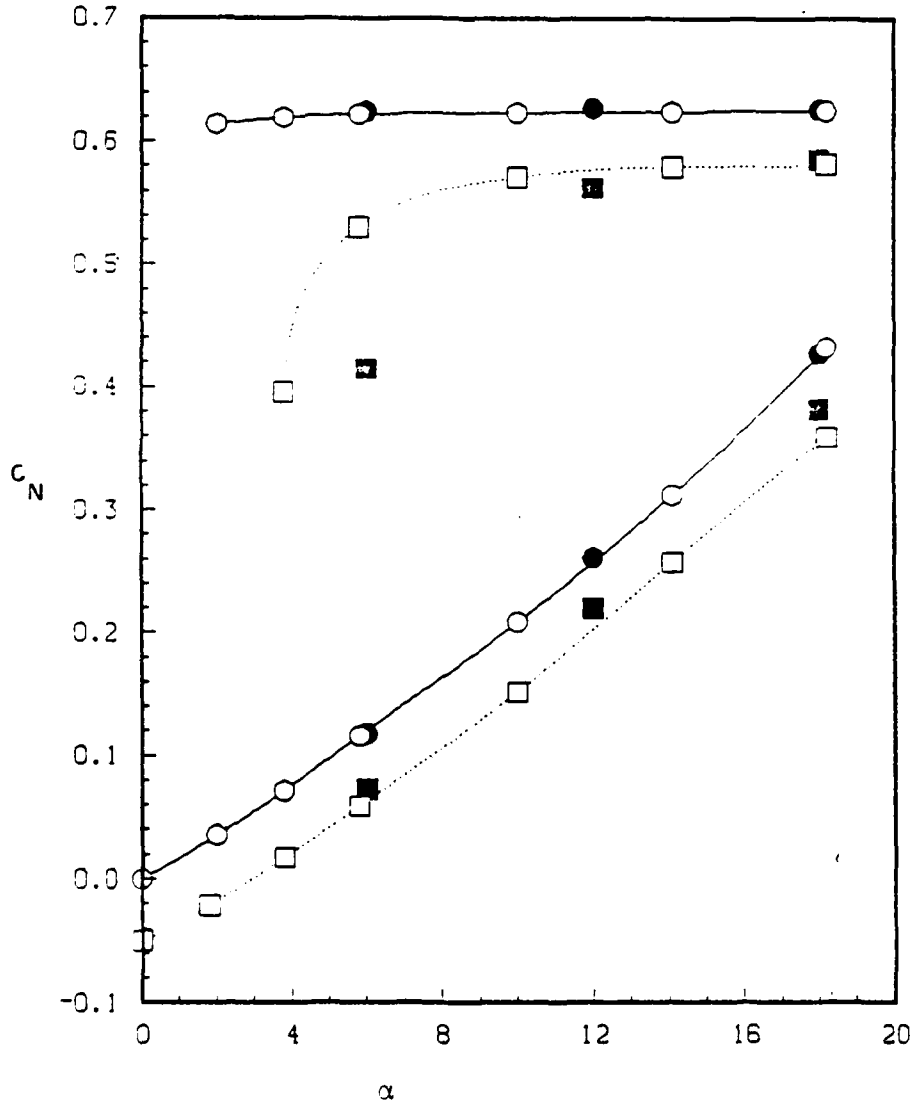

FIGURE 17. CALCULATED AND MEASURED NORMAL FORCE AND CENTER OF PRESSURE ON THE WING-BODY-TAIL MODEL REFERENCE 17

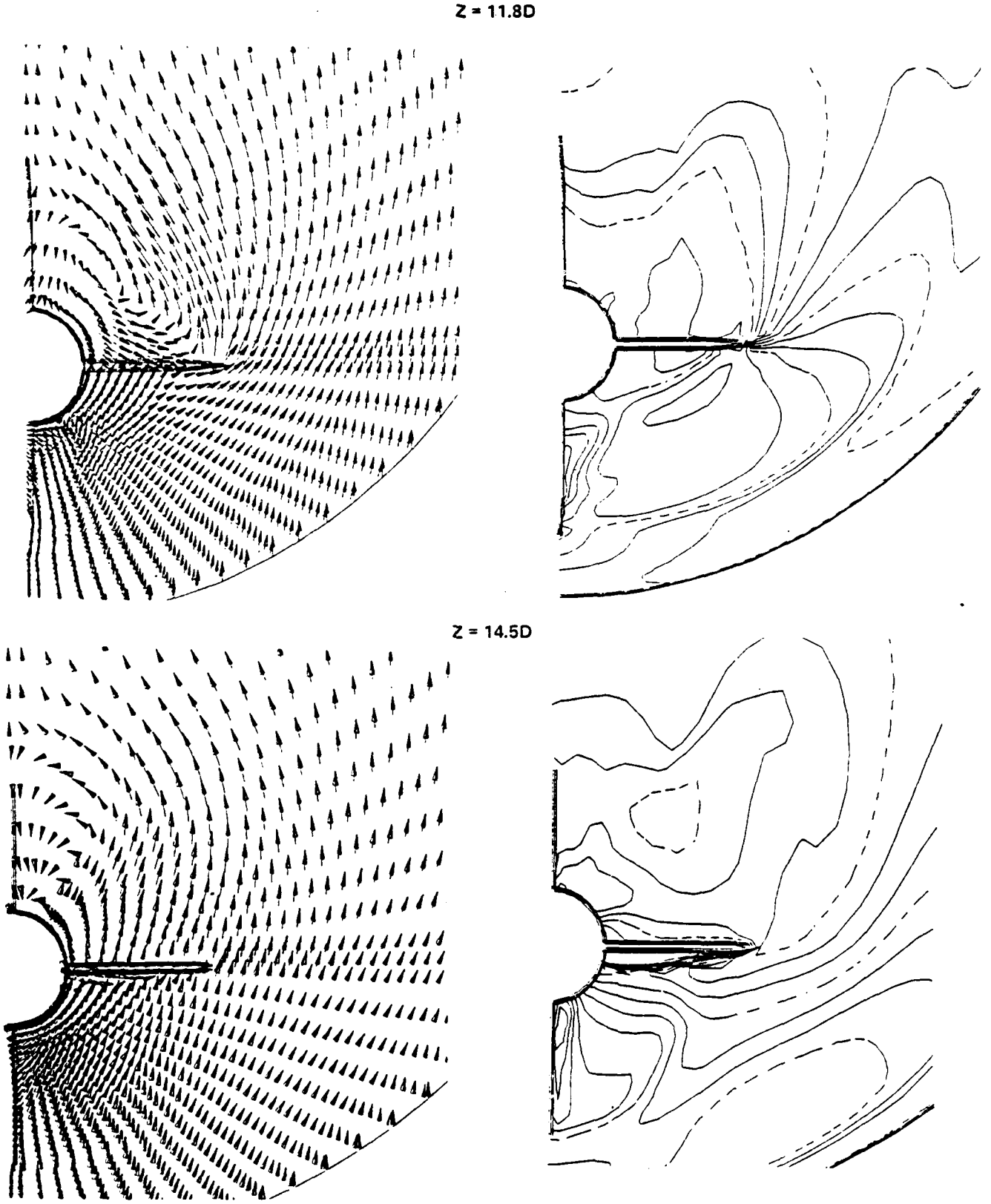

FIGURE 18. CROSSFLOW VELOCITIES AND PRESSURES ON THE MODEL OF FIGURE 17

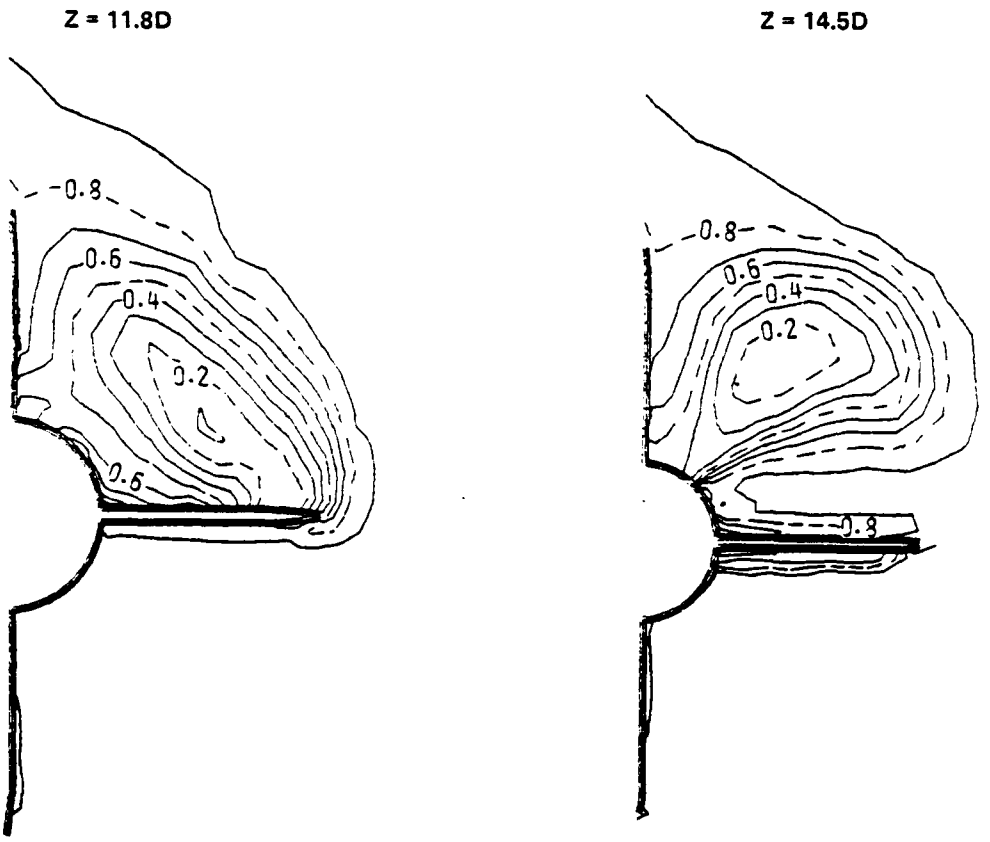

FIGURE 19. CROSSFLOW PLANE TOTAL PRESSURE (P_t/P_{t_∞}) ON THE MODEL OF FIGURE 17

TABLE 1. TYPES OF BOUNDARY CONDITIONS

TYPE	PURPOSE	EDGES ON WHICH ALLOWED
INTERIOR	PROVIDE FOR INTERFACING OF ADJACENT ZONES	2, 4
SYMMETRY	SIMULATE A SYMMETRY PLANE	2 OF ZONE 1 4 OF ZONE MAX*
FREESTREAM	IMPOSE FREESTREAM CONDITIONS AT END OF EACH STEP	ALL
SURFACE	SIMULATE A SOLID SURFACE	ALL
SHOCK	TRACK DOMAIN OF DEPENDENCE	3

* MAX - LARGEST ZONE NUMBER

REFERENCES

1. Wardlaw, A. B., Jr., Solomon, J. M., and Baltakis, F. P., "Supersonic Inviscid Computations for Missile Type Bodes," AIAA J., Vol. 19, No. 6, Jun 1981.

2. Wardlaw, A. B., Jr., Priolo, F. J., Solomon, J. M., and Baltakis, F. P., "Inviscid Multiple Zone Calculations for Supersonic Tactical Missiles," AIAA Paper 84-2099, Seattle, WA, Aug 1984.

3. Wardlaw, A. B., Jr., Baltakis, F. P., Martin, F. M., Priolo, F. J. and Dettmar, R. U., "Godunov's Method for Supersonic Tactical Missile Computations," Journal of Spacecraft and Rockets, Vol. 24, No. 1, Jan-Feb 1987, pp. 40-48.

4. van Albada, G. D., van Leer, B., and Roberts, W. W., Jr., "A Comparative Study of Computational Methods in Cosmic Gas Dynamics," Astro. Astrophys., Vol. 108, No. 76, 1982.

5. Colella, P., "A Direct Eulerian MUSCL Scheme for Gas Dynamics," SIAM J., Sci. Stat. Comput., Vol. 6, No. 1, Jan 1985, pp. 104-117.

6. Borrel, M. and Montage, J. L., "Numerical Study of a Non-Centered Scheme with Application to Aerodynamics," AIAA Paper No. 85-1497, Jul 1985.

7. Davis, S. F., "Simplified Second Order Godunov-Type Methods," to be published in SIAM JOURNAL ON SCIENTIFIC AND STATISTICAL COMPUTING.

8. Glaz, H. M., and Wardlaw, A. B., Jr., "A Higher Order Godunov Scheme for Steady Supersonic Gas Dynamics," JCP, Vol. 58, No. 2, Apr 1985, pp. 157-187.

9. Wardlaw, A. B., Jr., and Priolo, F. J., Applying the Second Order Godunov Code, NSWC TR 86-508, Dec 1986, Silver Spring, MD (to be published).

10. Osher, S., "Riemann Solvers, the Entropy Condition and Difference Approximations," SIAM J. Numerical Analysis, Vol. 21, 1984, pp. 217-235.

11. Harten, A., Lax, P. D. and van Leer, B., "An Upstream Differencing and Godunov-Type Scheme for Hyperbolic Conservation Laws," SIAM Review, Vol. 25, 1983, pp. 35-61.

12. Kordulla, W., and Vinokur, M., "Efficient Computation of Volume in Flow Predictions," AIAA J., Jun 1983, pp. 917.

13. Klopfer, G. H. and Nielsen, J. N., "Euler Solutions of the Body Vortices of Tangent Ogive Cylinders at High Angles of Attack and Supersonic Speeds," AIAA Paper 81-0361, AIAA 19th Aerospace Science Meeting, St. Louis, MO.

14. Landrum, E. J., "Wind-Tunnel Pressure Data at Mach Numbers from 1.6 to 4.63 for a Series of Bodies of Revolution at Angles of Attack from -4° to 60°," NASA TM X-3558, Oct 1977, NASA-Ames, Moffett Field, CA.

15. Lamb, M., Sawyer, W. B., Wassum, L. L., and Babb, C. D., "Pressure Distribution on Three Different Cruciform Aft-Tail Control Surfaces of a Wingless Missile at Mach 1.6, 2.36, and 3.78," Vol. II and III, NASA TM 80097, Aug 1979.

16. Jackson, C. M., Jr., and Sawyer, W. C., "A Method for Calculating the Aerodynamic Loading on Wing Body Combinations at Small Angles of Attack in Supersonic Flow," NASA TN D-6441, 1971.

17. Wardlaw, A. B., Jr., Priolo, F. J., and Solomon, J. M., An Inviscid Multiple Zone Method for Supersonic Tactical Missiles, NSWC TR 85-484, June 1986, Silver Spring, MD.

18. Spearman, M. L. and Sawyer, W. C., "Longitudinal Aerodynamic Characteristics at Mach Numbers from 1.6 to 2.86 for a Fixed-Span Missile with Three Wing Planforms," NASA TM 74088, Nov 1977, NASA Langley Research Center, Hampton, VA.

APPENDIX A

THE CFL CONDITION

The (CFL) condition requires that the domain of dependence of the numerical scheme contains the domain of dependence of the governing Partial Differential Equations, in this case the Euler equations. The domain of dependence of the Euler equations for some point P lies within the Mach cone with vertex at P. In the z = constant plane containing P, the domain of dependence is a point. Selecting z = constant planes which are at increasing distances from P, the size of the domain of dependence increases, as is illustrated in Figure A-1. The CFL condition prohibits step sizes in which the Mach cone covers any area outside of the finite difference stencil. The finite difference stencil is the area enclosed by lines connecting adjacent points whose information is used to advance properties at point P.

The trace of the Mach cone in a z = constant plane is illustrated in Figure A-2a. The shaded area represents the finite difference stencil of the lower order Godunov scheme. This stencil increases in size for the higher order scheme. However, near shocks and other steep gradients, the second order scheme degenerates to first order, and the CFL step size calculation must be based on the more restrictive first order domain of dependence.

Computation of the maximum allowable step size is more easily accomplished in computational coordinates where the grid is rectangular, as shown in Figure A-2b. As can be seen from this figure, the dimensions of the Mach cone cannot exceed l_1, l_2, l_3, l_4, in the $\bar{n}_1$, $\bar{n}_2$, $\bar{n}_3$, $\bar{n}_4$ directions respectively. Here l values are:

$$|l_i| = \bar{n}_1 \cdot (\pm \frac{\Delta\xi}{2}, 0, 0) = \frac{\Delta\xi\Delta\eta}{(\Delta\xi^2+\Delta\eta^2)^{1/2}} \quad , \qquad i = 1, 2, 3, 4 \quad \text{(A-1)}$$

where: $\Delta\xi = \xi$ mesh spacing
$\Delta\eta = \eta$ mesh spacing
$-$ sign applied to $i = 2,3$

while the $\bar{n}$ vectors are:

$$\begin{aligned} n_1 &= (\Delta\eta, \Delta\xi, n_{1_\zeta}) \\ n_2 &= (-\Delta\eta, \Delta\xi, n_{2_\zeta}) \\ n_3 &= (-\Delta\eta, -\Delta\xi, n_{3_\zeta}) \end{aligned} \quad \text{(A-2)}$$

$$n_4 = (\Delta n_1 - \Delta\xi,\ n_{4_\zeta})$$

The ζ component of each vector will be determined below by considering the definition of the Mach cone. Satisfaction of these four constraints assures that the CFL condition is met.

Satisfying the CFL condition requires determination of the maximum dimension of the Mach cone on a plane $\zeta = \zeta_Q$ in some direction, $\bar{n}$. As an example, consider direction $\bar{n}_1$ and define plane S with normal $\bar{n}_1$, to be tangent to the Mach cone. On the $\zeta = \zeta_Q$ plane, the point of tangency between S and the Mach cone is point T with coordinates $(K_1\Delta\zeta_Q+\xi_p,\ K_2\Delta\zeta_Q+\eta_p,\ \zeta_Q)$ as shown in Figure A-3. Here $(\xi_p,\ \eta_p,\ \zeta_p)$ are the coordinates of point P, $(K_1,\ K_2)$ are constants and $\Delta\zeta_Q = \zeta_Q - \zeta_p$. The Mach cone and plane S are tangent along a line TP with direction: $(K_1\Delta\zeta_Q,\ K_2\Delta\zeta_Q,\ \Delta\zeta_Q)$.

The minimum distance between the projection of P and S on plane $\zeta = \zeta_Q$ represents the maximum dimension, d_1, of the Mach cone in direction $\bar{n}_1$. It is computed as follows:

$$d_1 = \frac{(n_{1_\xi}, n_{1_\eta},\ 0)}{[n_{1_\xi}{}^2+n_{1_\eta}{}^2]^{1/2}} \cdot [K_1\Delta\zeta_Q,\ K_2\Delta\zeta_Q,\ \Delta\zeta_Q] = \frac{[n_{1_\xi}K_1+n_{1_\eta}K_2]\Delta\zeta_Q}{[n_{1_\xi}{}^2+n_{1_\eta}{}^2]^{1/2}} \qquad \text{(A-3)}$$

Since $\bar{n}_1$ is perpendicular to the Mach cone and the vector TP: $(K_1\Delta\zeta_Q,\ K_2\Delta\zeta_Q,\ \Delta\zeta_Q)$ lies on the surface of the Mach cone. Then:

$$\bar{n}_1 \cdot (K_1\Delta\zeta_Q,\ K_2\Delta\zeta_Q,\ \Delta\zeta_Q) = 0 \Rightarrow n_{1_\xi}K_1 + n_{1_\eta}K_2 = -n_{1_\zeta} \qquad \text{(A-4)}$$

and substituting Eq. (A-4) into Eq. (A-3) yields:

$$d_1 = \frac{-n_{1_\zeta}\Delta\zeta_Q}{(n_{1_\xi}{}^2+n_{1_\eta}{}^2)^{1/2}} \qquad \text{(A-5)}$$

To satisfy the CFL condition

$$|d_1| < |\ell_1|. \qquad \text{(A-6)}$$

Substituting the definition of ℓ_1, d_1 from Eqs. (A-2) and (A-5) respectively into Eq. (A-6) yields:

$$|\Delta\zeta| < \frac{\Delta n\Delta\xi}{|n_{1_\zeta}|} \qquad \text{(A-7)}$$

To complete the calculation of the CFL condition based on direction $\bar{n}_1$, it is necessary to determine values of n_{1_ξ}, n_{1_η} and n_{1_ζ} which are consistent with the definition of the Mach cone. In (x, y, z) space, the Mach number normal to the Mach cone surface is unity. Thus if $\bar{n}_1$ is to be normal to the Mach cone, it must satisfy the condition:

$$(\bar{n}_1 \cdot \bar{q})^2 - a^2|\bar{n}_1|^2 = 0 \qquad \text{(A-8)}$$

This condition can be transformed to computational space (ξ, η, ζ) using the chain rule applied to the components of $\bar{n}_1$,

$$n_{1_x} = n_{1_\xi}\xi_x + n_{1_\eta}\eta_x$$

$$n_{1_y} = n_{1_\xi}\xi_y + n_{1_\eta}\eta_y$$

$$n_{1_z} = n_{1_\xi}\xi_z + n_{1_\eta}\eta_z + n_{1_\zeta}$$

Substituting the above into Eq. A-8 yields:

$$a^2[n_{1_\xi}\nabla\xi + n_{1_\eta}\nabla\eta]^2 + a^2 n_{1_\zeta}^2 + 2n_{1_\zeta}a^2[n_{1_\xi}+n_{1_\eta}] - [n_{1_\xi}U+n_{1_\eta}V+n_{1_\zeta}w]^2 = 0 \qquad \text{(A-9)}$$

where: $U = \nabla\xi \cdot \bar{q}$

$V = \nabla\eta \cdot \bar{q}$

$\nabla\xi = \xi_x\underline{i} + \xi_y\underline{i} + \xi_z\underline{k}$

$\nabla\eta = \eta_x i + \eta_y j + \eta_z k$

The ξ and η components of vector $\bar{n}_1$ have previously been specified as $\Delta\eta$ and $\Delta\xi$, respectively. Substituting these values into the above, yields a quadratic equation for the ζ component. Solving for $n_{1_\zeta}/\Delta\xi$ produces:

$$\frac{n_{1_\zeta}}{\Delta\xi} = \left|\delta(a^2\xi_z - wU) + (a^2\eta_z - wV)\right| + a\{(w\xi_z - U)^2 + \delta^2(w\eta_z - V)^2$$

$$+ (w^2 - a^2)[\delta^2(\xi_x^2 + \xi_y^2) + (\eta_x^2 + \eta_y^2)] + 2\delta[(w\xi_z - U)(w\eta_z - V)$$

$$+ (w^2 - a^2)(\eta_x\xi_x + \eta_y\xi_y)]\}^{1/2} / (w^2 - a^2)$$

where: $\delta = |\Delta n/\Delta \xi|$

Here the positive root is taken and the absolute value of the quantity outside the radical is used to assure that the largest possible magnitude for n_{1_ζ} has been obtained.

To determine the maximum possible step size, the above calculation must be repeated for the remaining three directions. The resulting expression for the CFL condition is as follows:

$$\Delta\zeta = \frac{(w^2 - a^2)\Delta n}{\delta c_1 + c_2 + [a^2\{c_3\delta^2 + c_4 + c_5\delta]^{1/2}}$$

where: $c_1 = |a^2\xi_z - wU|$

$c_2 = |a^2 n_z - wV|$

$c_3 = (w\xi_z - U)^2 + (w^2 - a^2)(\xi_x{}^2 + \xi_y{}^2)$

$c_4 = (wn_z - V)^2 + (w^2 - a^2)(n_x{}^2 + n_y{}^2)$

$c_5 = 2|(w\xi_z - U)(wn_z - V) + (w^2 - a^2)(n_x\xi_x + n_y\xi_y)|$

$\delta = \Delta n/\Delta\xi$

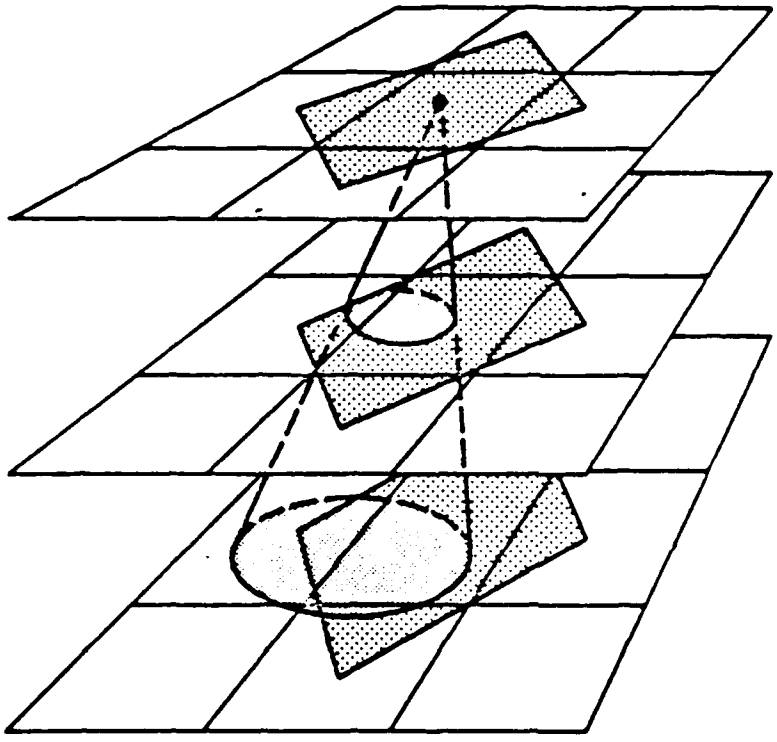

FIGURE A-1. PERMISSIBLE STEP SIZE BASED ON THE CFL CONDITION

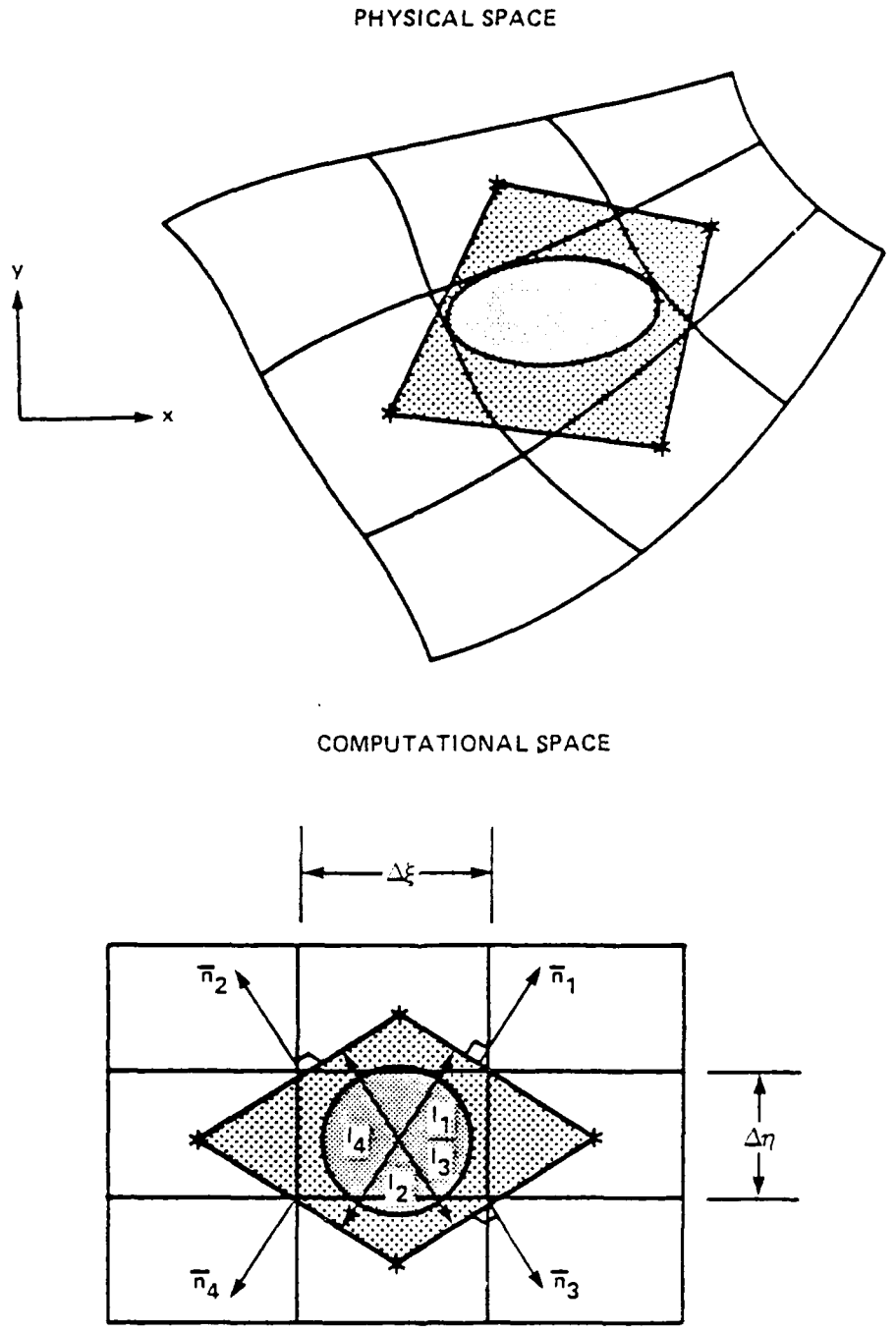

FIGURE A-2. MACH CONE TRACE AND FINITE DIFFERENCE STENCIL OF FIRST ORDER GODUNOV SCHEME

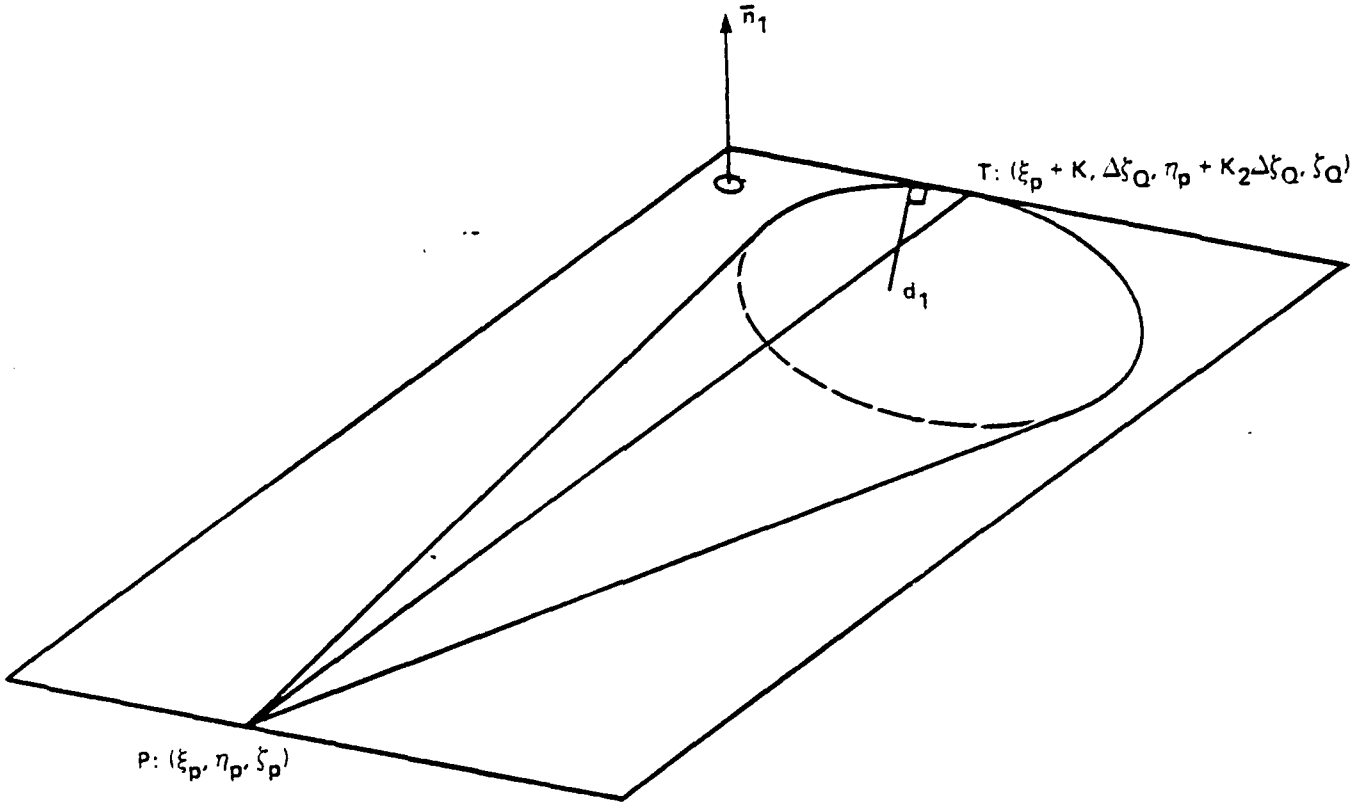

FIGURE A-3. MACH CONE AND TANGENT PLANE WITH NORMAL $\bar{n}_1$

DISTRIBUTION

	Copies
Commander Naval Sea Systems Command	
Attn: AIR310C (Mr. D. Hutchins)	1
SEA 62R41 (Mr. L. Pasiuk)	1
Technical Library	1
Washington, DC 20362	
Chief of Naval Material	
Attn: Mr. S. Jacobson (MAT 032)	1
Dr. John Huth	1
Technical Library	1
Washington, DC 20362	
Commander Naval Air Systems Command	
Attn: AIR 320C	1
AIR-530 (S. Loezos)	1
AIR5223D1 (D. A. DiPietro)	1
Technical Library	1
Washington, DC 20361	
Commander Naval Weapons Center	
Attn: Mr. R. Van Aken	1
Mr. R. Estes	1
Mr. F. A. Mansfield	1
Mr. R. Burman	1
Mr. R. E. Smith	1
Technical Library	1
China Lake, CA 93555-6001	
Commander Pacific Missile Test Center	
Attn: Mr. J. Rom	1
Mr. G. Cooper	1
Technical Library	1
Point Mugu, CA 93041	

	Copies
Commander David W. Taylor Naval Ship Research and Development Center	
Attn: Dr. J. Shott	1
Technical Library	1
Washington, DC 20007	
Commander Office of Naval Research	
Attn: Dr. T. C. Tai	1
Technical Library	1
800 N. Quincy St. Arlington, VA 22217	
Commanding Officer Naval Air Development Center	
Attn: Mr. W. Tseng	1
Technical Library	1
Warminster, PA 18974	
Superintendent U. S. Naval Academy	
Attn: Head, Weapons Dept.	1
Head, Science Dept.	1
Dr. A. Maddox	1
Technical Library	1
Annapolis, MD 21402	
Superintendent U. S. Naval Postgraduate School	
Attn: Technical Library	1
Monterey, CA 95076	
Officer in Charge Naval Intelligence Support Center	
Attn: NISC-4211 (J. B. Chalk)	1
Technical Library	1
4301 Suitland Road Washington, DC 20390	

DISTRIBUTION (Cont.)

	Copies
Commanding Officer Naval Ordnance Station Attn: Technical Library Indian Head, MD 20640	1
Director, Development Center Marine Corps Development and Education Center Quantico, VA 22134	1
Chief of S and R Division Development Center Marine Corps Development and Education Center Quantico, VA 22134	1
Commanding General Ballistic Research Laboratory Attn: Dr. W. Sturek Mr. C. Nietubicz Technical Library Aberdeen Proving Grounds, MD 21005	1 1 1
Commanding General ARRADCOM Picatinny Arsenal Attn: Mr. H. Hudgins Mr. G. Friedman Mr. W. Gadomski Mr. T. Hoffman Technical Library Dover, NJ 07801	1 1 1 1 1
Commanding General U. S. Army Missile R & D Command DROMI-TDK Redstone Arsenal Att: Dr. D. J. Spring Dr. C. D. Mikkelsen Technical Library Huntsville, AL 35809	1 1 1
Commanding Officer Armament R & D Center U. S. Army AMCCOM Attn: SMCAR-AET-A (Mr. J. Grau) Dover, NJ 07801-5001	1
Commanding Officer Harry Diamond Laboratories Attn: Technical Library Adelphi, MD 20783	1
Arnold Engineering Development Center Attn: Mr. J. Usselton Mr. W. B. Baker, Jr. USAF, Tullahoma, TN 37389	1 1
Commanding Officer Air Force Armament Laboratory Attn: Dr. D. Daniel Mr. C. Butler Mr. K. Cobb Mr. C. Mathews Mr. E. Sears Mr. F. Stevens Dr. L. E. Lijewski Lt. Bruce Haupt Eglin Air Force Base, FL 32542	1 1 1 1 1 1 1 1
USAF Academy Attn: Technical Library Colorado Springs, CO 80912	1
Commanding Officer Air Force Wright Aeronautical Laboratories (AFSC) Attn: Dr. V. Dahlem Mr. Dick Smith Mr. E. Brown-Edwards Mr. Gary O'Connell Wright-Patterson Air Force Base OH 45433	1 1 1 1
Defense Advanced Research Projects Agency ATTN: Technical Library Department of Defense Washington, DC 20305	1
Defense Intelligence Agency Attn: DIAC/DT-4A (Mr. P. Murad) Washington, DC 20301	1

DISTRIBUTION (Cont.)

	Copies
NASA Ames Research Center	
Attn: Dr. G. Chapman	1
Mr. V. L. Peterson	1
Technical Library	1
Moffett Field, CA 94035	
NASA Langley Research Center	
Attn: Mr. Jerry Allen	1
Mr. J. South	1
Mr. L. Spearman	1
Mr. W. C. Sawyer	1
Dr. J. Townsend	1
Technical Library	1
Langley Station	
Hampton, VA 23365	
Virginia Polytechnic Institute and State University	
Dept. of Aerospace Engineering	
Attn: Dr. J. A. Schetz	1
Dr. C. H. Lewis	1
Technical Library	1
Blacksburg, VA 24060	
North Carolina State University	
Department of Mechanical and Aerospace Engineering	
Attn: Dr. F. R. DeJarnette	1
Technical Library	1
Box 5246	
Raleigh, NC 27607	
The University of Tennessee Space Institute	
Attn: Dr. J. M. Wu	1
Mr. C. Balasubramayan	1
Technical Library	1
Tullahoma, TN 37388	
University of Notre Dame	
Department of Aerospace and Mechanical Engineering	
Attn: Dr. R. Nelson	1
Technical Library	1
Box 537	
Notre Dame, IN 46556	

	Copies
Applied Physics Laboratory	
The John Hopkins University	
Attn: Dr. L. L. Cronvich	1
Mr. Roland E. Lee	1
Mr. Michael White	1
Dr. Dave Van Wie	1
Technical Library	1
John Hopkins Road	
Laurel, MD 20810	
Raytheon Company	
Missile Systems Division	
Attn: Mr. D. P. Forsmo	1
Mr. P. A. Giragosian	1
Dr. Hugh T. Flomenhoft	1
Technical Library	2
Hartwell Road	
Bedford, MA 01730	
McDonnell-Douglas Astronautics Co. (East)	
Attn: Mr. J. Williams	1
Mr. S. Vukelich	1
Mr. M. I. Adiasor	1
Technical Library	1
P. O. Box 516	
St. Louis, MO 61366	
McDonnell-Douglas Astronautics Co. (West)	
Attn: Dr. J. Xerikos	1
Technical Library	1
5301 Bolsa Avenue	
Huntington Beach, CA 92647	
Lockheed Missiles & Space Co., Inc.	
Attn: Dr. D. Andrews	1
Technical Library	1
P. O. Box 1103	
Huntsville, AL 35807	
Lockheed Missiles & Space Co., Inc.	
Attn: Dr. Lars E. Ericsson	1
Mr. P. Reding	1
Mr. H. S. Shen	1
Technical Library	1
P. O. Box 504	
Sunnyvale, CA 94086	

DISTRIBUTION (Cont.)

	Copies
Nielsen Engineering & Research, Inc.	
Attn: Gary Kuhn	1
510 Clyde Ave.	
Mountain View, CA 95043	
General Electric Co.	
Armament Systems Department	
Attn: Mr. R. Whyte	1
Burlington, VT 05401	
CAL SPAN Advanced Technology Center	
Attn: Mr. B. Omilian	1
P. O. Box 400	
Buffalo, NY 14225	
Northrop Services, Inc.	
Attn: W. Boyle	1
Huntsville, AL 35810	
Vought Corporation	
Attn: Mr. F. Prillman	1
Dr. W. B. Brooks	1
Mr. R. Stancil	1
Mr. M. Worthy	1
P. O. Box 225907	
Dallas, TX 75265	
Hughes Aircraft Corporation	
Missiles Systems Group	
Attn: Dr. J. Sun	1
Technical Library	1
8433 Fallbrook Ave.	
Canoga Park, CA 91304	
Sandia Laboratories	
Attn: Mr. R. La Farge	1
Mr. R. Eisler	1
Mr. W. H. Rutledge	1
Mr. W. Wolfe	1
Technical Library	1
Albuquerque, NM 87115	
Martin Marietta Aerospace	
Attn: Mr. F. G. Aiello	1
Mr. R. Cavalleri	1
Mr. Mike Shoemaker	1
Technical Library	1
P. O. Box 5837	
Orlando, FL 23855	

	Copies
Business & Technology Systems, Inc.	
Attn: Dr. J. B. Eades, Jr.	1
Suite 400, Aerospace Building	
10201 Greenbelt Road	
Seabrook, MD 20801	
Lawrence Livermore Laboratory	
Earth Sciences Division	
Attn: Mr. D. G. Miller	1
Technical Library	1
University of California	
Livermore, CA 94550	
Honeywell, Inc.	
Attn: Mr. S. Sopszak	1
Technical Library	1
600 Second Street	
Minneapolis, MN 55343	
Pacifica Technology	
Attn: Dr. H. T. Ponsford	1
P. O. Box 148	
Del Mar, CA 92014	
Rockwell International	
Missile Systems Division	
Attn: Mr. J. E. Rachner	1
Technical Library	1
4300 E. Fifth Ave	
P. O. Box 1259	
Columbus, OH 43216	
Boeing Computer Services, Inc.	
Attn: Mr. R. Wyrick	1
P. O. Box 24346	
Seattle, WA 98124	
Motorola Inc.	
Missile Systems Operations	
Attn: Mr. G. H. Rapp	1
8201 East McDowell Road	
P. O. Box 1417	
Scottsdale, AZ 85252	
Douglas Aircraft Co.	
Aero Research, 36-81	
Attn: Dr. T. Cebeci	1
Long Beach, CA 98046	

DISTRIBUTION (Cont.)

	Copies
United Technologies Research Center Attn: David Sobel East Hartford, CT 06108	1
The Garrett Corp. Attn: G. J. Amarel Dr. William Jackonis 1625 Eye St., N.W. Washington, DC 20006	1 1
Boeing Aerospace Company Attn: William Herling (MS 82-23) P. O. Box 399 Seattle, WA 98124	1
Antonio Ferri Laboratories Attn: Dr. A. M. Agnone Merrick & Stewart Avenues Westbury, NY 11590	1
Marquardt Attn: T. Piercy (MS 84-1) 16555 Santicoy Street Van Nuys, CA 91409	1
United Technology Chemical System Attn: Warren Anderson 600 Metcalf Road San Jose, CA 95138	1
Morton Thiokol, Inc. Attn: A. M. Freed (M/S 223) P. O. Box 524 Brigham City, UT 84302	1
Grumman Aerospace Corp. Research & Development Center Attn: Dr. M. J. Siclari Mail Stop A 08-35 Bethpage, NY 11714	1
ACUREX Croporation Aerotherm Division Attn: John P. Crenshaw 555 Clyde Avenue P. O. Box 7555 Mountain View, CA 94039	1
Boeing Military Airplane Co. Attn: David Mayer P. O. Box 3707 Mail Stop 41-52 Seattle, WA 98124	1
Goodyear Aerospace Corp. Defense Systems Division Attn: A. L. Dunne 1210 Massillon Road Akron, OH 44315	1
General Dynamics/Pomona Division Aerothermodynamics (MA 4-87) Attn: Mr. G. Meyers P. O. Box 2507 Pomona, CA 97169	1
General Dynamics/Convair Division Aerodynamics (M.Z. 55-6950) Attn: Mr. David Brower P. O. Box 85357 San Diego, CA 92138	1
AAI Attn: Dr. T. Stasny Cockeysville, MD 21030	1
Integrated Systems, Inc. Missile Division Attn: Michael Briggs 151 University Ave. Palo Alto, CA 94301	1
TRW Space & Technology Group Attn: Dr. T. Shivananda One Space Park Redondo Beach, CA 90278	1
General Electric Co. Computational Aerodynamics Technology Attn: Dr. James Daywitt P. O. Box 7722 Philadelphia, PA 19101	1

DISTRIBUTION (Cont.)

	Copies
Physical Research, Inc. Attn: Mr. Rudy Swigart 655 Deep Valley Drive Suite 320 Palos Verdes, CA 20274	1
Science Applications International Corp. Attn: Mr. Darryl W. Hall 994 Old Eagle School Road Suite 1018 Wayne, PA 19087	1
Defense Technical Information Center Cameron Station Alexandria, VA 22304-6145	12
Library of Congress Attn: Gift & Exchange Div. Washington, DC 20390.	4
EG&G Washington Analytical Services Center, Inc. Attn: Technical Library P. O. Box 552 Dahlgren, VA 22448	1
NASA Attn: Technical Library Washington, DC 20546	1

Internal Distribution:	Copies
G23 (Moore, Devan, Hase)	3
K22	1
K24	1
R44 (Wardlaw)	30
R44 (Priolo)	30
E231	2
E232	15

END

FEB.

1988

DTIC